Controlled Electrochemical Synthesis Of Giant Magnetostrictive Iron-Gallium Alloy Thin Films And Nanowires

A dissertation

submitted to the faculty of the Graduate School

of the University of Minnesota

by

KOTHA SAI MADHUKAR REDDY

in partial fulfillment of the requirements

for the degree of

Doctor of Philosophy

Bethanie J. H. Stadler, Adviser

April 2012

Acknowledgments

This work would never have been possible without the generous help of a number of people:

First and foremost, my mom Bhagyasri: for setting a powerful example through her life with uncompromising honesty and integrity; for not praising my little successes to sky-high limits, instead reminding me that life is not about competing with the world, but a constant and dogged, and sometimes seemingly dull, pursuit of excellence for its own sake; for not pitying me when things went horribly wrong, but demanding me to work harder and smarter instead of succumbing to despair.

my sister Kavitha: for being such an amazing support to me throughout my life. I am truly blessed to have a sister like her, and if there is one quality of hers that I have tried to emulate during the course of my PhD, then it is her fight-unto-death-and-beyond attitude!

Stephanie: for being such a fabulous friend, philosopher and guide! A constant source of encouragement through the many ups-and-downs during the course of last several years, she taught me the virtue of a balanced approach to life's cycle of successes and failures. It is beyond doubt that her friendship has been the secret behind such a joy-filled PhD!

Beth: I am really fortunate to have had such a wonderful person as my advisor! Her constant encouragement and admirable patience, especially during the initial learning stages, really mattered a lot. For the kind of freedom that she gave me in pursuing my research, I will always be very grateful for the confidence she had in me. In more ways than one, I feel I have become a better person and researcher after having worked with Beth.

Swadesh Srivastava: for being such an all-weather and a true friend, almost like a brother I never had!

My heartfelt thanks to Prof. Alison Flatau, Dr. Jung Jin Park and Dr. Suok-Min Na at the University of Maryland for such a friendly and fruitful collaboration.

Prof. William H. Smryl: for his enthusiastic willingness to discuss any research problem that I had, and also for his active interest in my work. Dr. Dong-Ha Lim for his generous help in familiarizing me with the Rotating Disk Electrode.

My wonderful team-members Mazin, Anirudh, Sang-Yeob, Xiaobo, Eliot, Andy, Matt.

Special thanks to professors Paul Crowell, Chris Palmstrøm, Andre Mkhoyan, and Bharat Jalan for highly useful discussions and generous encouragement.

Dedication

Dedicated with love and respect to my dearest mom Bhagyasri and sister Kavitha

Abstract

Magnetostrictive Galfenol ($Fe_{1-x}Ga_x$, x = 10% - 40%) alloys have generated tremendous interest in recent times because of their potential as functional materials in various micro- and nano-electromechanical systems (MEMS/NEMS)-based transducers and sensors. Among the giant magnetostrictive alloys, Terfenol-D ($Tb_{1-x}Dy_xFe_2$) has the largest magnetostriction, but its brittle nature limits its applications. In contrast, the next best magnetostrictive alloy, Galfenol, is highly malleable and ductile while having the tensile strength of Iron. Electrochemistry is an economical route to fabricate 'very thick' films (upto several microns) or high-aspect ratio structures like nanowire arrays. However, the highly electropositive nature of gallium makes it very difficult to electrodeposit from aqueous solutions, similar in behavior to other non-ideal elements like molybdenum, phosphorus, tungsten etc. As a result, $Fe_{1-x}Ga_x$ alloy plating has been severely plagued by non-repeatability in compositions from growth to growth, lack of uniformity in filling of pores when growing nanowires in nanoporous templates, undesired secondary hydrogen evolution reactions etc.

In this study, a thorough understanding of the complex interplay between various deposition parameters (pH, overpotential, concentration, hydrodynamic conditions) was achieved, leading to an understanding of the deposition mechanism itself, thus allowing excellent control and ability to tune the alloy compositions. Arrays of nanowires were fabricated with alternating segments of the magnetostrictive alloy $Fe_{1-x}Ga_x$ and Cu in nanoporous anodic aluminum oxide (AAO) templates. A novel rotating disk electrode-template (designed in-house) was used to optimize the nanowire length distributions by controlling the various aspects of electrodeposition like nucleation, kinetics and mass-transfer. Extensive structural characterization was done by X-ray diffraction

(XRD), electron backscatter diffraction (EBSD) and transmission electron microscopy (TEM), and magnetic characterization by vibrating sample magnetometry (VSM).

Furthermore, of excellent promise in semiconductor spintronics, the feasibility of fabricating epitaxially nucleated $Fe_{1-x}Ga_x$ thin films on GaAs having the desired (001) texture was demonstrated. Structural characterization using microdiffraction, high resolution ω - 2θ and rocking curve analysis revealed that the films grown on GaAs(001) are highly textured with <001> orientation along the substrate normal, and the texture improved further upon annealing at 300 °C for 2 hours in N_2 environment. This was in contrast to films grown on polycrystalline brass substrates which exhibited undesired <011> texture out-of-plane. Rocking curve analysis on $Fe_{1-x}Ga_x$/GaAs structures further confirmed that the <001> texture in the $Fe_{1-x}Ga_x$ thin film was indeed due to epitaxial nucleation and growth. A non-linear current-voltage plot was obtained for the $Fe_{1-x}Ga_x$/GaAs Schottky contacts, characteristic of tunneling injection, and showed improved behavior with annealing.

Table of Contents

List of Figures

CHAPTER 1: INTRODUCTION

1.1 Electrochemistry Background

When two dissimilar materials, say a metal and a solution, come in contact with each other, then in order to equilibrate the Fermi levels in both these phases (metal and solution) there is a transfer of charge between them until the Fermi levels match up. Such phenomena can be seen occurring in varied systems like metal-semiconductor junctions, semiconductor-semiconductor junctions and metal-solution interfaces. Here we are concerned with the final case: metal-solution interface.

When a metal electrode comes in contact with an electrolyte, it acquires some immobilized charge on its surface by one of three pathways: dissociation (of metal electrode atoms into its solvated ions), complexation, or adsorption (of ions from solution). This immobile charge on the surface attracts an exact number of excess ions from the liquid to shield the surface charge in order to make the interface neutral. This is the basic mechanism of formation of the so-called electrical "double layer" (Fig. 1).[5] It is emphasized that only one 'layer' of this double layer has strict definition, while the other is a 'diffused layer', as shown in the figure.

Fig. 1 illustrates schematically the electrical double layer. As discussed above, a plane of charge due to complexation or dissociation exists on the surface. For example, consider in this case that the total charge is negative on the electrode as shown. It may also be the case that ions from solution are specifically adsorbed, as shown by the negatively charged (bigger) blue spheres. The smaller blue spheres surrounding it represent the water dipoles, with the arrow pointing towards the negative side of the dipole (oxygen atom). Counterions (represented by green spheres, again shown hydrated) are attracted to the electrode surface by electrostatics, and help in shielding the surface charge. These counterions are not all in the same plane, however, because they are held in a dynamic balance by electrostatic attraction towards the interface (called ‘drift’) and the tendency to diffuse away from the interface (diffusion). The concentration of ions in the diffuse layer decays with distance from the surface. Thus the surface charge forms one layer and the diffuse shielding charge forms the other layer, hence the term "double layer". This double layer has a certain structure. The Inner Helmholtz Plane (IHP) is the plane cutting through the center of the adsorbed ions (in this case, anions). The Outer Helmholtz Plane (OHP) is the plane cutting through the positive ions at their positions of closest approach (determined by the size of the hydrating molecules, here water). Ions in the diffuse layer are always being exchanged at the surface, but the counterions always exactly balance the total charge associated with the interface. One consequence of this space charge distribution is that a position-dependant electrical potential within it exists which varies, as shown by the dotted white profile, from zero far from the surface and reaches a maximum magnitude very near the surface (to be specific, near the IHP). It will later be explained how this plays a role in electrodeposition.

Clearly the charged double layer is like a parallel-plate capacitor and is schematically represented in Fig. 1. When the capacitor is charged, a potential exists across the metal-solution interface (equal to charge/capacitance, or V=Q/C). This potential across the metal-solution interface is called the “Electrode potential”. Thus since every metal-solution system has its own characteristic capacitance and charge adsorption, a system is characterized by the voltage occurring across the double layer. The double layer width is generally taken as equal to the Debye length, which is the screening length. This Debye length is smaller for highly ionic solutions, and increases with temperature and dielectric constant of the medium.

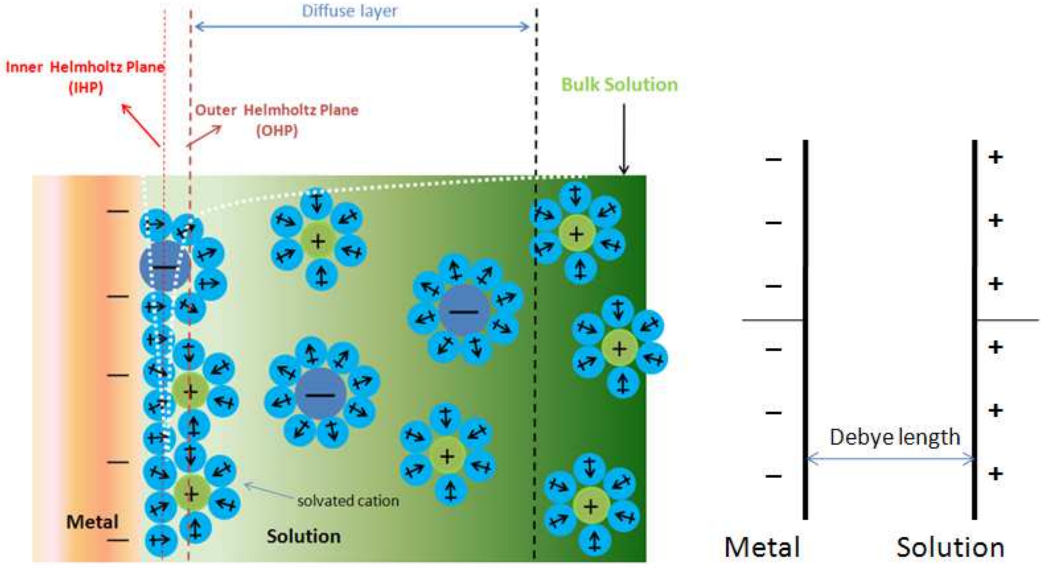

Fig. 1.1: (Left) Schematic of the electrical double layer occurring at metal-solution interfaces. Both the positive and negative ions are shown hydrated. (Right) Electrical equivalent of the Helmholtz double layer, a parallel-plate capacitor.

However, it is impossible to measure this intrinsic electrode potential for a given metal because to do so one would have to introduce another electrode into the system, but that will introduce its own electrode potential. To circumvent this, it is better if we choose by convention this second electrode and reference all electrode potentials to this ‘reference electrode’. And this is the case: all electrode potentials are referenced to a standard electrode called the Standard Hydrogen Electrode (SHE) whose potential is taken as zero (by convention). Furthermore, to form a series of such relative electrode potentials, one has to select standard conditions of components of the electrode/electrolyte interface for a given metal/metal-ion solution. Normally such standard conditions mean: the concentrations of the ions in the electrolyte is unity, the pressure of any gaseous phase is 1 bar, and the temperature of the cell is maintained at 25°C.

1.1.1 Electrochemical Deposition

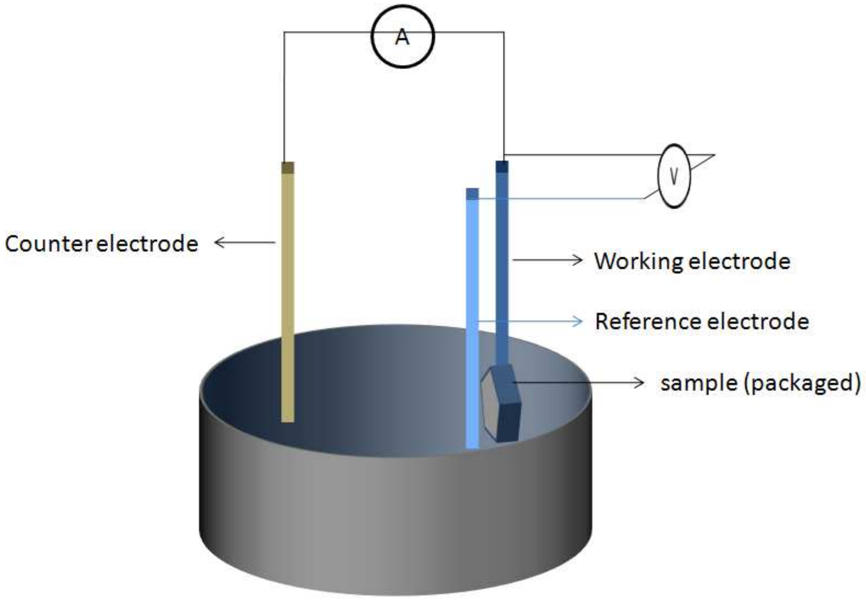

Fig. 1.2: A standard three-electrode electrochemical cell. Current is driven through the working electrode which is referenced against a standard electrode (like Ag/AgCl). While the ammeter measures the current being driven in the circuit, the voltmeter gives a real time measurement of the working electrode potential. Metal deposition occurs at the working electrode, while oxygen evolution occurs at the platinum counter electrode.

The electrode potentials mentioned above are all equilibrium potentials, that is, there is dynamic equilibrium at the metal-solution interface. However, when an electrode is made a part of an electrochemical cell through which current is flowing as in Fig. 2, its potential will differ from the equilibrium potential. Fig. 2 also shows a reference electrode against which the working electrode potential is measured, while the counter electrode completes the circuit. It should be noted that the reference electrode plays the role of a high impedance voltmeter that measures the potential without any current flowing through it.

If the equilibrium potential of the working electrode (that is, the potential in the absence of external current) is E and the potential of the same electrode as a result of external current flowing is E(I), the difference η between these two potentials, $\eta = E(I) - E$ is called overpotential. In electrodeposition, the overpotential η is required to overcome hindrance of the overall electrode reaction, which is usually composed of a sequence of partial reactions: charge-transfer, diffusion, chemical reaction and crystallization. For a given electrochemical reaction, one or more of them will act as the rate determining step, depending on the overpotential used. Fig. 3 depicts a typical current versus overpotential behavior when depositing Cu metal from a $CuSO_4$ bath. In this figure, at high overpotentials (and thus at the very high current densities), the electrochemical deposition rate is determined by how fast the Cu^{+2} ionic diffusion is replenishing the depleted interface double layer. That is, at these high overpotentials the reaction is diffusion limited.

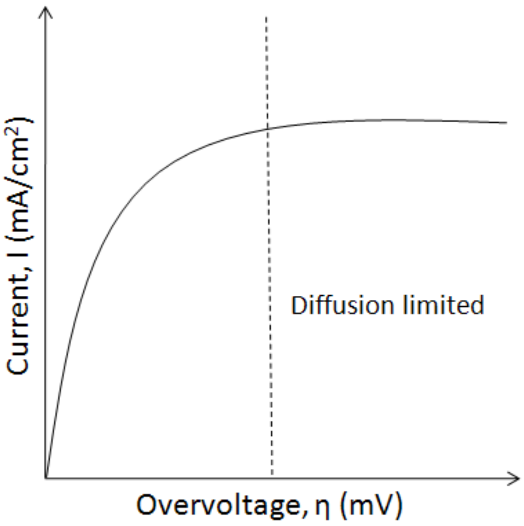

Fig. 1.3: A typical current versus applied overvoltage behavior. At low overpotentials, the current is linear as the metal deposition is limited mostly by charge transfer (how fast the electrode is giving electrons to the adsorbed metal ions). At higher overpotentials, the rate determining step now is how fast the ions are reaching the working electrode (that is, diffusion limited).

1.1.2 Nucleation and Growth of Electrodeposited Films

As with the case of other metal deposition techniques like sputtering or molecular beam epitaxy (MBE), parameters affecting the rate of nucleation and growth have a direct impact on the structure and morphology of the electrodeposited films.[5] As seen from Fig. 3, at intermediate overpotentials the deposition current starts to increase exponentially before reaching a steady-state diffusion-limited current density. Large current densities result in faster nucleation rates, and thus smaller sized nuclei, with the result that the grain size of the deposited films is smaller. Conversely, larger grain sizes occur for lower current densities and overpotentials.

However it should be mentioned that as the electrodeposited films grows thicker, it has been found that the average grain size increases resulting in columnar growth morphology. The microstructure change from relatively fine grains near the substrate to the columnar microstructure with much coarser grains at greater distances from the substrate are due to the growth competition between adjacent grains. The low-surface-energy grains grow faster than do the high-energy grains.

1.1.3 Texture in Electrodeposited Alloys

Electrodeposition even on a randomly oriented polycrystalline substrate can result in the development of preferred orientation/texture in thicker deposits. The root cause for this lies in the fact that different crystal faces of the grains in the growing film have different rates of growth. Thus, there is a growth rate competition between crystallites of various orientations. The type of texture depends on the composition of electrolyte and substrate, the overpotential, and other parameters. Thus controlling the growth parameters offers a unique opportunity to tailor the material morphology to suit our desired material properties.

1.2 Electrochemical Template Synthesis of Nanowires

Nanowires with high aspect ratios can be fabricated either through standard lithography techniques or through electrochemical synthesis in nanoporous templates. While the throughput of the former is low, that of the latter is very high as well as being a very cheap process. Furthermore, vertical nanowires with varying diameters (from 5nm to more than 500nm) with lengths up to 100 μm can be produced by electrochemical deposition into the nanopores of a porous template. The electrochemical deposition of nanowire arrays was first reported in 1970 by Possin [6], who deposited tin nanowires in ion-track etched mica films. Since then, this method has been used to fabricate nanowires of metals, alloys, semiconductors, and electronically conducting polymers [7-13].

The method is relatively simple despite its large number of uses in different areas. A thin metal film is sputtered onto one side of a porous membrane, and this metal acts as the working electrode in a standard three-electrode electrochemical cell, as was shown in the Fig. 2.The nanowires form as the pores in the template are filled by the electrodeposited material. This technique can be used to synthesize not only single element nanowires, but also multi-element and/or multi-segment nanowires. An unrivalled advantage of the electrochemical template synthesis is the sheer number of monodisperse nanowires that one can produce.

Now what are the nanoporous templates made of? Templates for electrochemical deposition of nanowire arrays include porous AAO [14-23], etched nuclear particle tracks in various materials [24-29] and block copolymer films [30]. In this report, we concern ourselves primarily with AAO templates. The properties of the nanoporous template, such as the relative pore orientations in the assembly, the pore size distribution, and the surface roughness of the pores, have significant influence on the intrinsic properties of the nanowires. All these parameters can be controlled during AAO fabrication.

1.2.1 AAO Fabrication

Nanoporous alumina templates are formed by anodic oxidation of Al [14-23]. A schematic of a porous AAO template is shown in Fig. 4. Pore sizes (d) typically range from 20 to 250 nm and up to about 200 μm in thickness (d_{AAO}) [31]. This permits the fabrication of nanowires with aspect ratios more than 10^4. Pore densities typically range from 10^8 to 10^{10} cm^{-2}. With careful preparation, relatively large domains of hexagonally ordered pores can be achieved. Even longer-range ordering can be obtained by using nano-stamping techniques [22, 23].

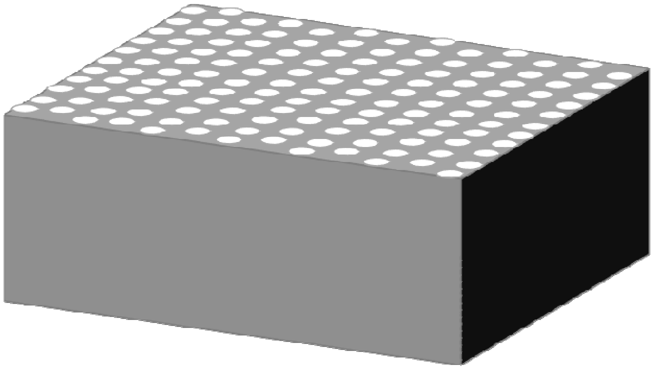

Fig. 1.4: A schematic of the geometry of the Anodized Aluminum Oxide (AAO) templates. Typical values are: pore diameter ranging from 20 nm – 250 nm; length of the pores upto 200µm.

1.2.2 Mechanism of Pore Growth

During the anodization process, a constant voltage is applied between the aluminum electrode (which acts as an anode) and the cathode (usually platinum). Therefore, the applied electric field lines lie perpendicular to the sample surface (anode) and are shown by blue lines in Fig. 6. However, at the pore bottom the electric field lines are radial, resulting in a higher electric field density there.

Oxidation of the Al metal occurs at the metal/barrier oxide interface by the migration of oxygen ions (O^{-2} or OH^{-}) from the electrolyte through the barrier layer by the following reaction [33]:

$2Al + 3O^{-2} \dashrightarrow Al_2O_3 + 6e$

A schematic representation of the ionic migration at the pore bottom under the applied electric field is given in Fig. 6. Furthermore, as discussed above, the applied electric field strength is enhanced at the pore bottom. This results in field enhanced dissolution of the barrier oxide layer, thus favoring pore growth. Dissolution of the oxide layer is caused mainly by the hydration reaction of the formed oxide layer as shown below [34]. It is to be noted that under the applied electric field the Al^{+3} ions migrate through the barrier oxide layer and into the electrolyte.

$2Al^{+3} + 3H_2O \text{-->} Al_2O_3 + 6H$

Loss of Al^{+3} ions in the electrolyte has been found to be a prerequisite for porous oxide growth. Thus at steady state, pore grows perpendicular to the Al surface when an equilibrium is established between the field enhanced dissolution of oxide layer at oxide/electrolyte interface and the oxide growth at metal/oxide interface [33]. Simultaneously, the alumina formation entails an expansion in the substrate and thus a competition for space ensues resulting in stress build-up. Due to this competition, there is a mutual 'repulsion' between the growing pores, which further enhances as well as dictates the ordering of the pores.

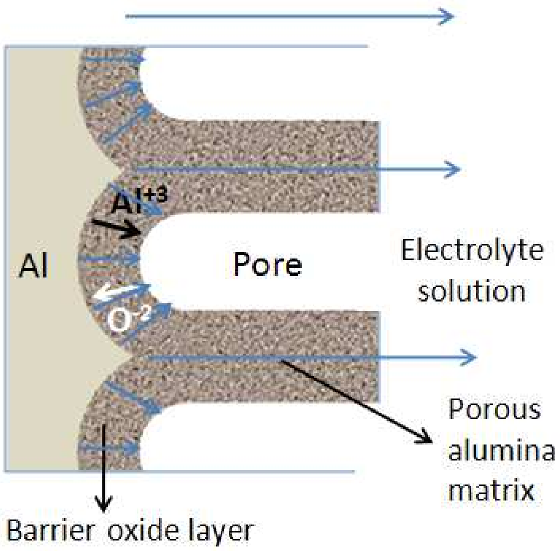

Fig. 1.6: A schematic of the mechanism for pore formation when Al metal is anodized. A thin barrier oxide layer always separates the parent Al metal and the nanopores. The pores grow in a self-assembled fashion owing to a mutual 'repulsion' due to stress build-up in the barrier layer [19].

1.2.3 Electrochemical Synthesis of Nanowires

Anodization of Al results in a nanoporous AAO template with a thin barrier layer sandwiched between the Al metal and the pores, as shown in Fig. 5(d) and Fig. 6. This is reproduced in top left of Fig. 7. One can continue the steps as shown in Fig. 5 to result in an AAO template with a metal contact layer on one side. Nanowires can be grown into these pores using DC electrodeposition (Fig. 7-right).

However, the removal of the barrier layer is not always feasible or desired (as will be seen in Future Work chapter). In such cases, one would have to be able to deposit nanowires into the nanopores with the barrier layer intact. This is in fact feasible by AC electrodeposition (Fig. 7-left). The barrier layer, even as it offers very high resistance under DC conditions, under AC conditions causes alternating positive and negative potentials at the barrier in contact with the electrolyte. Electrodeposition occurs during the cathodic half-cycle (negative part of the AC signal), without any dissolution during the anodic half-cycle [35]. A systematic study of the optimum growth conditions needed for uniform deposition in nanopores with a thin barrier layer is negative in Ref [36], where it has been found that using a pulsed AC waveform results in uniform deposition as compared to a continuous AC waveform.

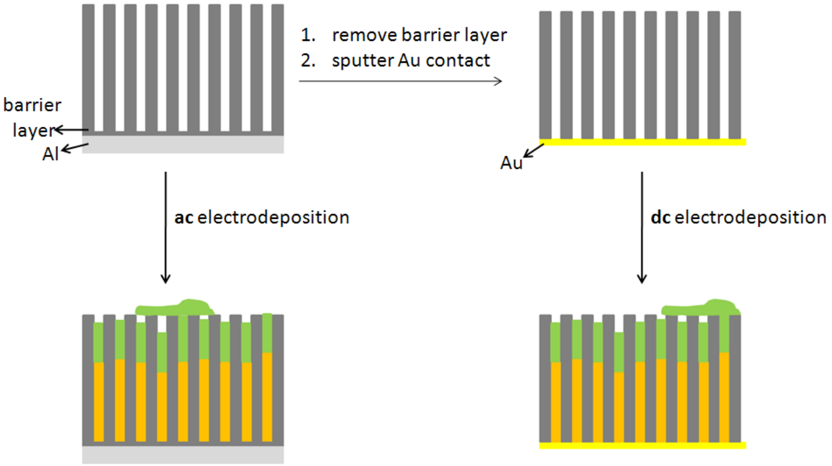

Fig. 1.7: (Left) Nanowire growth in an AAO template with barrier layer at the bottom is done using AC electrodeposition. (Right) Another way to grow nanowires is to use DC electrodeposition, but for that the barrier layer has to be removed and a contact layer deposited.

For both AC and DC electrodeposition, a typical current versus time curve is shown in Fig. 8. The initial current surge (i_{DL}) is due to the charging of the electrical double layer at the electrode-electrolyte interface. Once the voltage across the double layer is established (typically within a second), a steady current is established in Region I. As the nanowires come closer to the pore openings at the top, the current in Region I slightly increases. When a few nanowires come out of the pores in Region II, there is a surge in the current owing to the increased electrode area. In Region III, the deposition area is no longer increasing because the whole area has been covered. This results in a steady state current whose magnitude is dictated by diffusion limited conditions.

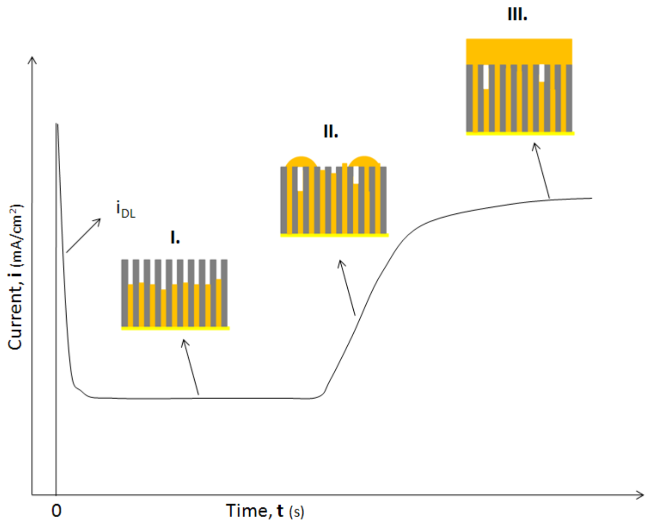

Fig. 1.8: Typical current vs time deposition curve during nanowire growths. i_{DL} is the current used to charge the electrical double layer setting up the voltage required for subsequent nanowire electrodeposition. Three growth regimes can be seen: (I.) nanowires grow inside the nanopores, (II.) a few nanowires start to grow out of the pores and as a result there is a sudden surge in the deposition current, and (III.) as the total surface is covered, a saturation current is reached that is diffusion limited.

1.3 Continuous Nanowires

Ferromagnetic nanowires, with which we will be concerned mostly, differ in the magnetic properties from their bulk and thin films forms. Magnetization hysteresis loops, which display the magnetic response of a magnetic sample to an external field, are used widely to characterize the behavior of nanostructured magnetic materials. Fig. 9 shows typical magnetization hysteresis loops obtained for an array of Fe-Ga nanowires, with the applied magnetic field parallel and perpendicular to the nanowire axis. The characteristic features of the hysteresis loop are dependent on the nanowire array characteristics: the material the nanowire is made up of, the size and shape of the nanowire, the microstructure, the angle between the applied magnetic field and the nanowire axis etc. For such arrays of nanowires, the hysteresis loop may also depend on interaction between individual wires in the template. The common parameters used to describe the magnetic properties are the saturation magnetization M_s, the remanent magnetization M_r, the coercivity H_c, and the saturation field H_{sat}.

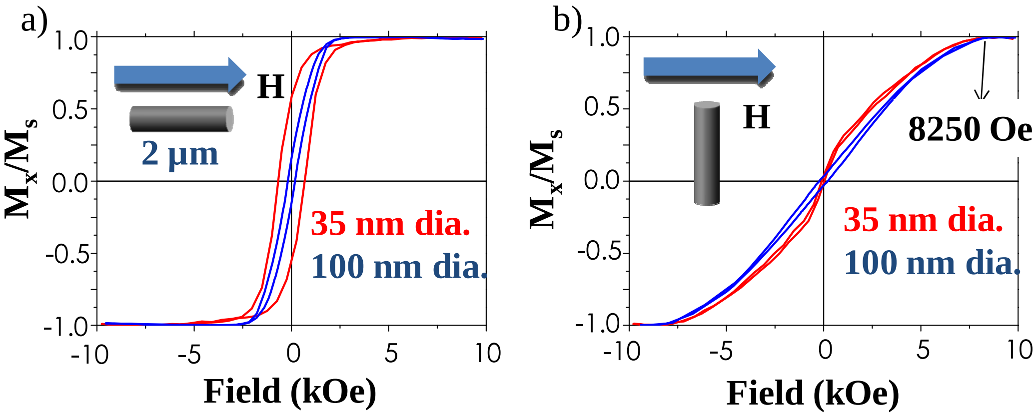

Fig. 1.9: Typical hysteresis loops for an array of $Fe_{80}Ga_{20}$ nanowires 2 µm long with the applied field H parallel (a) and perpendicular (b) to the wire axis.

The coercivity H_c is the applied field at which the magnetization M (measured along the direction of applied field) becomes zero; the saturation field H_{sat} is the field needed to reach the saturation magnetization M_s; and the remanent magnetization M_r is the inherent magnetization when there is no external applied field (that is, at H=0). For the case of magnetic nanowires H_c, H_{sat}, and M_r are strongly dependent on the size and shape of the wires as well as the angle between the nanowire and the applied magnetic field.

The saturation magnetization M_s is obtained when all magnetic moments in the material are aligned in the same direction. M_s is a property of the ferromagnetic material and hence is the only parameter that is independent of nanowire geometry.

Another parameter that is usually used to describe the magnetic property of a nanowire is the Curie Temperature. As the temperature of the ferromagnetic material is increased, thermal fluctuations can overcome the ordering of the magnetic moments in it. The temperature at which this transition from the ordered ferromagnetic state to the disordered paramagnetic state (with net magnetization zero) occurs is called the Curie temperature Tc, which is a property of the material as well as the nanowire shape and dimensions.

1.4 Multilayered Nanowires

Above we have concerned ourselves with the fabrication and characterization of single element nanowires. The magnetic properties of nanowires can be further tailored by incorporating multiple segments instead of just a single element, as shown in Fig. 10(a). The mechanical, magnetic and electrical properties of these ferromagnetic/non-magnetic multilayer nanowires can be tuned by varying their sizes, aspect ratios, and spacings of the ferromagnetic segments [37-46].

Now in the segments of these multilayer nanowires, one can have completely different elements or have the same elements but with differing stoichiometry. Electrodeposition of the latter type of nanowires is achieved, from a solution containing the ions of the two components, by modulation of the potential or current. This results in the deposition of a compositionally modulated multilayer with a bilayer repeat unit of the form A_xB_{1-x}/ A_yB_{1-y}. Systems that have been studied include CuBi [47], CuZn [48], NiMo [49], AgPd [49] and AuAg [50]. In these systems, the composition all modulation was relatively small, typically less than 30 at.%.

However, a major breakthrough in multilayer deposition occurred when it was recognized that multilayers of the form B/A (with very little of A in B) can be obtained for systems for which the difference in equilibrium potentials between A and B is sufficiently large (typically >0.4V) and the concentration of the more noble component is very low. This approach has been successfully exploited in the deposition of nanowires with alternating ferromagnetic and non-magnetic layers that exhibit GMR (ref). Examples of electrodeposition of FM/NM multilayers include Ni/Cu [51-55], Co/Cu [56-59], CoNi/Cu [60-62], and NiFe/Cu [63, 64].

CHAPTER 2: ELECTROCHEMICAL DEPOSITION MECHANISMS

2.1 Introduction

Giant magnetostrictive $Fe_{1-x}Ga_x$ alloys, because of their excellent magneto-mechanical coupling [1], promise exciting applications in a variety of microelectromechanical (MEMS) and nanoelectromechanical (NEMS)-based devices [2, 3]. Electrochemical deposition (ECD) as a method of fabricating the $Fe_{1-x}Ga_x$ alloys, in both thin film and nanowire forms, has been a focus of vigorous research in recent years (see [4] and references therein). ECD not only provides an economical route, but also is uniquely suited to deposit conformal and 'thick' films (up to several 10's of microns) that are necessary in applications requiring magnetostrictive materials [3]. However, gallium is very difficult to electrodeposit from aqueous solutions [5], similar in behavior to other elements like Mo, W, Rh etc [6]. Several studies have determined that the deposition of these elements can only be induced in the presence of transition elements like Fe [7-10]. Even though electrochemical deposition of Fe-Ga alloys from citrate electrolytes was first demonstrated in 2005 [11], the deposition mechanism has not been fully understood [4, 12]. As a result, reproducible and controllable electrodeposition of $Fe_{1-x}Ga_x$ alloys has so far been elusive. To make things more complicated, secondary hydrogen evolution reactions often accompany the deposition [4, 12], presenting immense challenges especially during fabrication of nanowires inside nanoporous templates.

Detailed investigations into the complex interplay between various deposition parameters (pH, overpotential, concentration) have led to important insights which have been critical to recent successes in exerting remarkable control over deposition not only of $Fe_{1-x}Ga_x$ thin films [13], but also $Fe_{1-x}Ga_x$/Cu multilayered nanowire arrays [14, 15]. This study presents the key insights, and while throwing light on the deposition mechanism of the $Fe_{1-x}Ga_x$ alloys, also demonstrates a precise control over thin film composition in the entire range of interest (15% - 30% Ga) [1].

2.2 Experimental Details

2.2.1 Electrochemical Cell

A conventional three-electrode cell was used with a platinum strip as counter electrode, and a saturated calomel electrode (SCE) as reference (with a Luggin capillary). The working electrode was a Gamry Instruments rotating disk electrode (RDE) with electrode tips made of vitreous carbon and brass (78.9 mm^2 area). The brass electrode-holder was redesigned so that, after electrodeposition, the electrode tip could be loaded into a scanning electron microscope (SEM) for compositional and morphological characterization. Immediately before each electrochemical measurement, the carbon electrode surface was polished with alumina, cleaned with methanol, ultrasonicated in DI water, again cleaned with methanol, and then rinsed with DI water. The brass electrode surface was subjected to an additional diamond polishing step. A scan rate of 5 mV/s was used for linear sweep voltammetry (LSV). During chronoamperometry (CA), a fixed potential was applied, and the current density was monitored as a function of time. Compositional analysis was done using energy dispersive spectroscopy (SEM-EDS).

2.2.2 Electrolytic solution

Two types of electrolytes were used: ‘Fe(II)-Ga(III)’ and ‘Fe(II)’. The former binary electrolyte consisted of 0.065 M Na_3-citrate, 0.5 M Na_2SO_4, 0.015 M $FeSO_4$, and 0.038 M $Ga_2(SO_4)_3$ (mixed in the same order). The latter ‘Fe(II)’ electrolyte consisted of 0.065 M Na_3-citrate, 0.6875 M Na_2SO_4 and 0.015 M $FeSO_4$ (extra Na_2SO_4 was added so that both electrolytes had the same ionic strength). While ‘Fe(II)-Ga(III)’ electrolyte was used to study Fe-Ga electrodeposition, the

‘Fe(II)’ electrolyte was used to empirically evaluate the diffusion coefficient of Fe(II) ions ($D_{Fe(II)}$). Electrolyte pH was adjusted to 3.8 using NaOH. The electrolyte was purged with N_2 gas throughout the mixing process, followed by 15 minute purging between experiments.

2.3 Results and Discussion

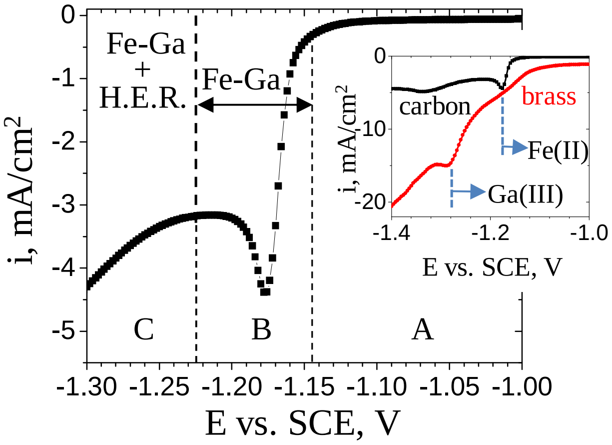

Fig. 2.1: Linear Sweep Voltammetry (LSV) under quiescent conditions. LSV curve obtained for $Fe_{1-x}Ga_x$ *electrodeposition on a carbon rotating disk electrode (RDE). (inset) Full-range LSV curves obtained on carbon and brass RDE. Indicated are potentials where Fe(II) and Ga(III) ions become transport-limited.*

Fig. 1 shows LSV curve obtained on a carbon RDE under quiescent conditions using Fe(II)-Ga(III) electrolyte. While no significant reduction reactions occurred in regime A, the deposition peak in regime B corresponded to $Fe_{1-x}Ga_x$ deposition. No discernible secondary hydrogen evolution reactions were observed in either regime A or B, but visibly occurred in regime C (along with $Fe_{1-x}Ga_x$ deposition). Clearly, $Fe_{1-x}Ga_x$ deposition in regime B was under mixed transport and activation control. The inset in Fig. 1 shows large-scale LSV curves obtained on carbon and brass electrodes. Also indicated in the inset are potentials where Fe(II) and Ga(III) ions became diffusion-limited.

Chronoamperometric (i vs t) plots were obtained on carbon RDE at various potentials chosen from within regime B of Fig. 1, with the rotation rates (ω) being varied between 0 rpm and 1800 rpm. One such set of curves obtained at -1.225 V are shown in Fig. 2a. At each value of ω, the *steady-state* current (i_{ss}) was a combination of mass-transfer (i_{mt}) and kinetics-limited current densities (i_k). The Koutecky - Levich (K-L) equation gives an expression for the combined steady-state current density (i_{ss}) [16]:

$$i_{ss}^{-1} = i_{mt}^{-1} + i_k^{-1} = (b_{RDE}^{-1})\, \omega^{-1/2} + i_k^{-1} \tag{1}$$

$$\text{with } b_{RDE} = 0.62\, nFC_bD^{2/3}v^{-1/6} \tag{2}$$

where, n is the number of electrons taking part in the overall reaction, F the Faraday constant, C_b the bulk concentration of reducing ions, D the diffusivity, v the kinematic viscosity.

2.3.1 Mass-transport

K-L plots (i_{ss}^{-1} vs $\omega^{-1/2}$) obtained for various potentials chosen from regime B of Fig. 1 are shown in inset of Fig. 2b. From the slopes of the K-L plots, one may evaluate b_{RDE} values (see Eq. 1) at each potential. However, this by itself is of limited use because in the expression for b_{RDE} (Eq. 2), values of C_b, n or D are not readily apparent for the Fe(II)-Ga(III) binary solution. In order to obtain typical values for D, the above experiments were repeated with ‘Fe(II)’ solution (in this case, n = 2, and $C_b = C_b^{Fe(II)}$ = 15 mM). K-L plots were plotted for the Fe(II) system (not shown), and an average value of $D_{Fe(II)} = 1.8 \times 10^5$ cm^2/s was obtained. Now, for the Fe(II)-Ga(III) binary solution, it may be assumed that the Ga(III) and Fe(II) ions have a similar value for D as

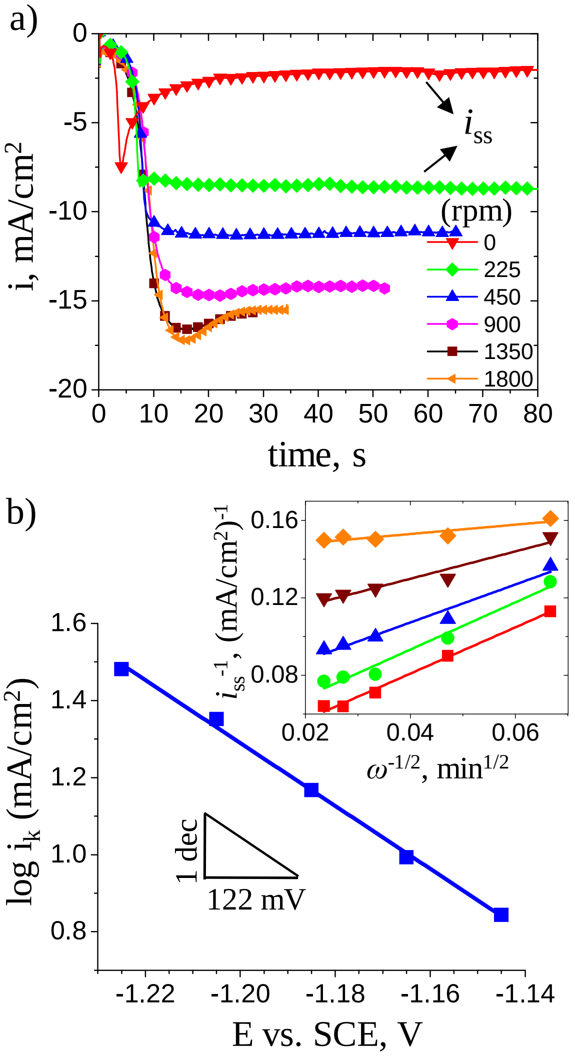

Fig. 2.2: Steady-State electrochemistry at a carbon RDE. a) Chronoamperometric curves obtained at various rotation rates (at a fixed potential of -1.225 V). Numbers indicate rotation rate in rpm. b) Tafel plot obtained for various potentials chosen from within regime B in Fig. 1. (inset) Corresponding Koutecky-Levich plots that were used to construct the Tafel plot. In the inset, (♦) -1.145 V, (▼) -1.165 V, (▲) -1.185 V, (●) -1.205 V, (■) -1.225 V.

calculated for the Fe(II) solution above, and furthermore that $n \approx 2.25$ (corresponding to an average composition of $Fe_{75}Ga_{25}$). Using these values in the expression for b_{RDE}, an average value of $C_b \approx 16$ mM was obtained for the Fe(II)-Ga(III) solution. Incidentally, this value was very close to the bulk concentration of Fe(II) ions in the Fe(II)-Ga(III) binary solution, suggesting that it was the Fe(II) ions that play a determinant role in the electrodeposition of $Fe_{1-x}Ga_x$ alloys, at least in the mixed transport-activation controlled regime B.

2.3.2 Kinetics and Deposition Mechanism

Pure kinetics-limited current density (i_k) values were calculated from y-intercepts of the K-L plots (Fig. 2b inset). Using these i_k values, a Tafel plot (Fig. 2b) was obtained that had an inverse slope of 122 mV dec^{-1}. The fact that the Tafel slope had a value close to 120 mV dec^{-1} indicated that a two-step reduction mechanism was operative during Fe-Ga deposition, which is characteristic for the iron-group metals Fe, Ni and Co [17]. Following a deposition mechanism proposed for induced co-deposition of Fe-Mo alloys [7], we propose the following mechanism for Fe-Ga system.

$$\mathrm{Fe(II)} + e^- \rightarrow [\mathrm{Fe(I)}]_{ads} \qquad \text{(I)}$$

$$[\mathrm{Fe(I)}]_{ads} + e^- \rightarrow \mathrm{Fe(s)} \qquad \text{(IIa)}$$

$$[\mathrm{Fe(I)}]_{ads} + \mathrm{Ga(III)} \dashrightarrow [\mathrm{Ga(III)\text{-}Fe(I)}]_{ads} \qquad \text{(IIb)}$$

$$[\mathrm{Ga(III)\text{-}Fe(I)}]_{ads} + 3e^- \rightarrow \mathrm{Ga(s)} + [\mathrm{Fe(I)}]_{ads} \qquad \text{(IIc)}$$

The first step (Eq. I), also the rate determining step [17], involves a partial reduction of Fe(II) (which in reality involves a complex with H_2Cit^-) into an adsorbed intermediate $[Fe(I)]_{ads}$. In the second fast step, this very unstable $[Fe(I)]_{ads}$ adsorbed complex follows one of two possible routes: it is further reduced to metallic Fe(s) (as in Eq. IIa) or it *induces* the reduction of Ga(III) by first forming a mixed [Ga(III)-Fe(I)]$_{ads}$ adsorbed intermediate (Eq. IIb), followed by reduction to metallic Ga(s) (Eq. IIc).

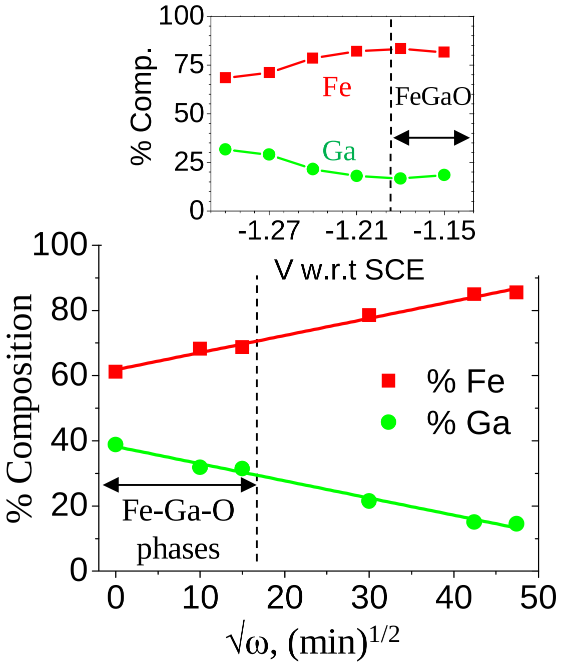

Fig. 2.3: Fe$_{1-x}$Ga$_x$ thin films on brass RDE. Variation of composition as a function of rotation rate at a fixed potential of -1.24 V. (inset) Variation of composition as a function of potential at 900 rpm.

In order to confirm the induced co-deposition of Ga in the presence of Fe, Fe$_{1-x}$Ga$_x$ thin films were deposited on brass RDE, and the resultant composition was studied independently as a function of applied potential (inset of Fig. 3) and rotation rate (Fig. 3). From the inset of Fig. 3, it can clearly be seen that gallium always reduced along with Fe, confirming induced codeposition.

Next, thin films were deposited at a potential of -1.24 V so that Ga(III) ions were still under activation control but Fe(II) ions were under transport control (see brass LSV in inset of Fig. 1). Fig. 3 shows the obtained thin film composition plotted in the form of a Levich plot, that is, as a function of $\sqrt{\omega}$. The linear relationship is a clear indication that Fe-Ga composition was indeed determined by the transport of Fe(II) ions. In other words, the competition for free surface sites by the two types of intermediates, $[Fe(I)]_{ads}$ and $[Ga(III)\text{-}Fe(I)]_{ads}$, determined the relative reaction rates between Eqs. IIa and IIb, and in turn determined the partial current densities i_{Fe} and i_{Ga}.

Careful analysis revealed that thin films deposited at low potentials or low rotation rates consisted of Fe-Ga-oxide phases (see Fig. 3). While low potentials may have resulted in only a partial reduction of Ga(III) to Ga(I) or Ga(II), ineffective agitation at low rotation rates may have led to a local rise in pH - both cases leading to formation of low-valency gallium-oxides instead of complete reduction to metallic gallium. Remarkably, however, by simultaneously controlling deposition potential and convection, 15% - 30% Ga metallic alloys were obtained, which spans the entire range of compositions where $Fe_{1-x}Ga_x$ alloys are known to be highly magnetostrictive [1]. In fact, a cantilever capacitance bridge [18,19] was used to measure the magnetostriction of electroplated $Fe_{1-x}Ga_x$ films for the first time in this study, and it was found that $Fe_{80}Ga_{20}$ films of 330 nm thickness had a saturation magnetostriction of 112 ppm.

2.4 Conclusions

A deposition mechanism for $Fe_{1-x}Ga_x$ alloys was proposed in which the formation of an adsorbed monovalent $[Fe(I)]_{ads}$ intermediate was considered to be the rate-determining step. In subsequent steps, this intermediate either gets reduced to iron or catalyses the reduction of gallium by forming an adsorbed $[Ga(III)\text{-}Fe(I)]_{ads}$ intermediate. In fact, induced codeposition of gallium *requires* the formation of this adsorbed intermediate with iron. In line with the proposed mechanism, differences in the mass-transport rates of Fe(II) and Ga(III) species affected the extent of reactions IIa and IIb, so that by controlling the rotation rate alone, metallic thin film compositions in the entire range of interest (15% - 30% Ga) were obtained.

CHAPTER 3: SIMULATIONS OF NANOWIRE GROWTH

3.1 Simulations versus Experimental Conditions

An electrochemical system consists of two electrodes, and a third reference electrode. While the chemical reactions of interest occur at the 'working electrode', the other 'counter electrode' typically plays the role of completing the electrical circuit if spaced far apart. Furthermore, a counter electrode that has a larger area compared to the working electrode has a smaller current density than the working electrode, and thus the overpotential there is very small and time invariant. In addition, a highly conductive solution has negligible ohmic potential drop inside the solution, and the overpotential on the working electrode is then equal to the potential applied to the electrochemical cell.

However, real experiments do not come close to the ideal case presented above, and hence there is a need to take practical conditions into consideration. That is, one has to consider that the counter electrode is an essential part of the experiment, and thus parameters like its finite area, and the corresponding electrochemical reactions occurring there might have an effect on the overall behavior of the electrochemical cell. Thus a model, which considers both electrodes in equal detail, is needed. In this chapter, taking the above into consideration, a simulation of Chronoamperometry as well as Cyclic Voltammetry at microelectrode arrays is considered using COMSOL 3.5a simulation software.

3.2 Simulation of Electrodeposition in Microelectrode Arrays

The basic relationship between the cell current and the voltage applied for the electrode reaction $O + n\ e^- \leftrightarrow R$, where both oxidized (O) and reduced (R) species are soluble in the solution, is given by the current-overpotential equation (Brett and Brett)

$$I_e = I_{e,0}\left[\frac{c_R(0,t)}{c_R^b}\, e^{k\alpha_{e,a}\eta_e} - \frac{c_O(0,t)}{c_O^b}\, e^{-k\alpha_{e,a}\eta_e}\right] \tag{1}$$

where I_e is total cell current (A), $I_{e,0}$ the exchange current (A), c_O the concentration of oxidized species (mol/m^3), c_R the concentration of reduced species, C^b_R the bulk concentration of the species, $\alpha_{e,a}$ the anodic apparent transfer coefficient, $\alpha_{e,c}$ the cathodic apparent transfer coefficient, η_e surface overpotential of electrode (V), k=nF/RT with n being the number of electrons, F the Faraday constant, R the ideal gas constant, and T the absolute temperature. Above, the reaction (1) in question is considered to be of first order, meaning that the reaction rate is assumed linearly proportional to the concentration of the species. In the above equation, the surface overpotential η is defined as $\eta = [\varphi_{app} - V - \varphi_{eq}]$ where φ_{app} is the applied potential, V is the potential inside the solution just outside the diffusion layer, and φ_{eq} is the potential if the electrode was at equilibrium.

With the above construct, a COMSOL simulation model was developed that simulates the electrodeposition of copper in a micro-array electrode. The model is thorough in that it takes into consideration the deformation of the simulation geometry (cathode grows while the anode etches away) as the electrodeposition occurs. This is accomplished by the use of moving mesh application mode available in the COMSOL 3.5a simulation software. Using the software, Chronoamperometry and Cyclic Voltammetry have been modeled.

3.2.1 Model Definition

The model simulates the electrodeposition of copper from an aqueous copper sulfate bath. The solution has such low pH that the concentration of [H$^+$] ions is very low compared to that of the copper and sulfate ion concentrations, and thus we need only to consider the copper and sulfate ions, in the absence of any simultaneous reactions like hydrogen evolution at cathode or oxygen evolution at anode. That is, we need only consider the deposition of copper at the cathode and simultaneous dissolution of copper anode as Cu^{+2} ions. That is, the electrode reactions are assumed to take place with 100% efficiency. Furthermore, sulfate ion is treated as a fully dissociated ion. Finally, any plausible free convection at the electrodes arising out of the electrode reactions is completely neglected.

Dependent and Independent Variables in the Model

The model is clearly time dependent because both the electrode boundaries deform as a result of the electrode reactions. The four fundamental equations in electrochemistry allow us to solve for all the four unknowns in the problem (these four unknowns being current density and potential distribution in solution, and the copper and sulfate ion concentrations). An additional relationship between external applied potential and the current density (the Butler Volmer relation) allows us to relate the independent variable (applied potential, φ_{app}) and the other dependent variables discussed above. Yet another relation between the current and the amount of material being deposited allows us to track the deformation of the mesh, thus allowing us to simulate the electrochemical process completely.

3.2.2 Simulation Geometry and Boundary Conditions

The various geometries used in the model are depicted in Fig. 1. The parameters being considered in the simulation are the pore lengths, and the interpore separation. With the pore separation being held constant at 8.5µm, the pore lengths used are 0.5 µm, 5 µm and 10 µm. The last geometry is compared to an interpore separation of 4.25 µm.

The upper boundary represents the anode, while the cathode is placed at the bottom. The vertical walls are considered insulating which also happens to be a symmetry boundary condition. Now the actual equations need to be arrived at. The flux for each of the ions in the electrolyte is given by the Nernst Planck equation

$$N_i = -D_i \nabla c_i - u_i z_i F c_i \nabla \emptyset_i \tag{2}$$

where N_i denotes the 2-D flux vector, c_i the concentration of the ion in the electrolyte, z_1 the charge on the ion, u_i the mobility of the ion, F Faradays constant, and φ_i the potential in the electrolyte.

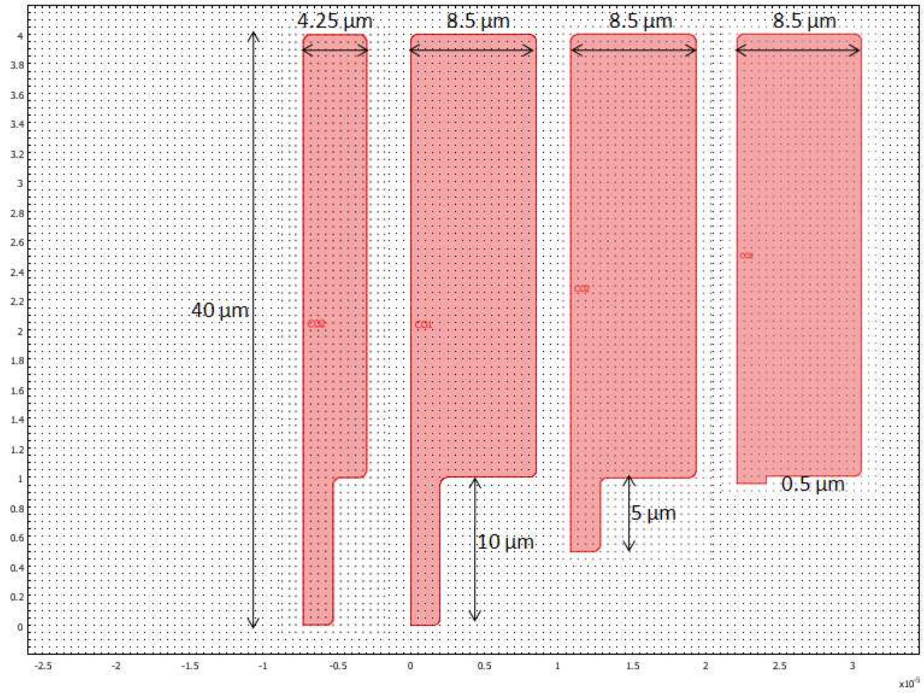

Fig. 3.1: Various geometries considered in the simulation. Parameters varied, as shown, are pore length and interpore separation.

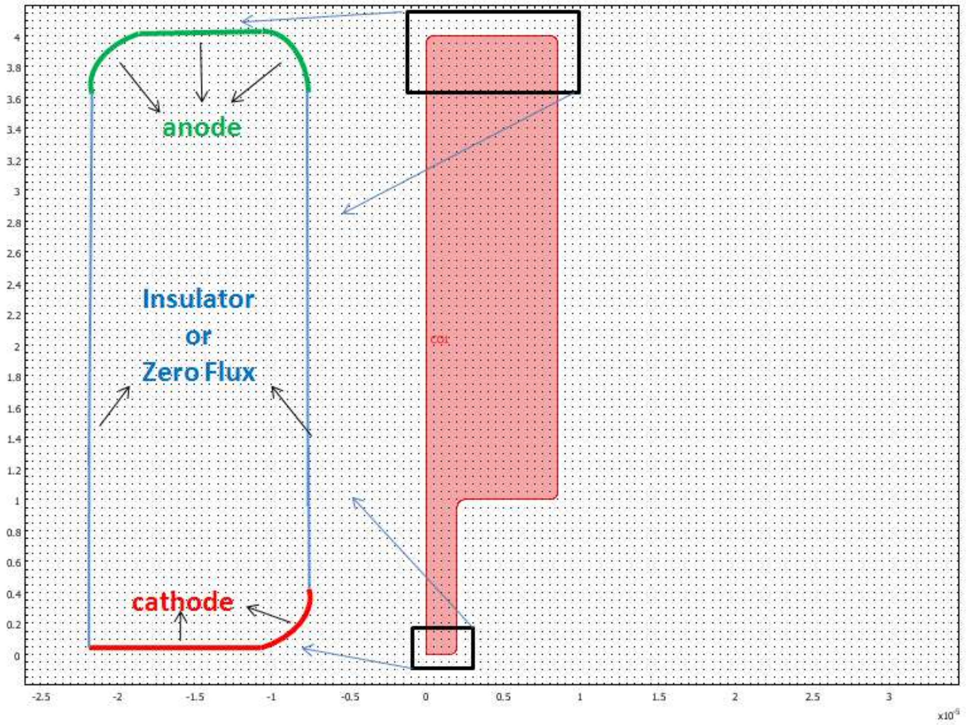

Fig. 3.2: Boundary conditions used.

The rate of change of ionic concentration is related to the flux in the absence of any homogenous reactions as

$$\frac{dc_i}{dt} + \nabla . N_i = 0 \tag{3}$$

Electroneutrality condition gives:

$$\sum_i -z_i c_i = 0 \tag{4}$$

As mentioned earlier, the boundary conditions for the anode and cathode are given by the Butler-Volmer equation (Eq. 1). Copper electrodeposition is assumed to take place through a two step mechanism:

$$Cu^{+2} + e^- = Cu^+$$

$$Cu^+ + e^- = Cu$$

where the first step is rate determining step (RDS) which is assumed to be at equilibrium. From Brett and Brett, the following relation between the local current density as a function of potential and copper concentration can be obtained:

$$i_{ct} = i_0\left(exp\left(\left(\frac{1.5F\eta}{RT}\right) - \frac{c_{Cu^{+2}}}{c_{Cu^{+2},ref}}exp\left(-\frac{0.5F\eta}{RT}\right)\right)\right) \tag{5}$$

where η denotes the overpotential as defined earlier.

This gives the following condition for the cathode

$$N_{Cu^{+2}}\,.\ n = -\frac{i_0}{2F}\left(\left(exp\left(\frac{1.5F(\emptyset_{s,cat}-\emptyset_1-\Delta\emptyset_{eq})}{RT}\right) - \frac{c_{Cu^{+2}}}{c_{Cu^{+2},ref}}exp\left(-\frac{0.5F(\emptyset_{s,cat}-\emptyset_1-\Delta\emptyset_{eq})}{RT}\right)\right)\right) \tag{6}$$

where n denotes the normal vector to the boundary.

A similar condition at the anode is

$$N_{Cu^{+2}}\,.\ n = -\frac{i_0}{2F}\left(\left(exp\left(\frac{1.5F(\emptyset_{s,an}-\emptyset_1-\Delta\emptyset_{eq})}{RT}\right) - \frac{c_{Cu^{+2}}}{c_{Cu^{+2},ref}}exp\left(-\frac{0.5F(\emptyset_{s,an}-\emptyset_1-\Delta\emptyset_{eq})}{RT}\right)\right)\right) \tag{7}$$

All other boundaries are taken as insulating to simulate symmetry conditions

$$N_{Cu^{+2}}\,.\ n\ =\ 0 \tag{8}$$

For the sulfate ions, insulating conditions apply everywhere

$$N_{{SO_4}^{-2}}\,.\ n\ =\ 0 \tag{9}$$

The initial condition set the composition of the electrolyte according to:

$$c_{Cu^{+2}} = 0$$

$$c_{SO_4{}^{-2}} = 0$$

Equations 3 through 9 are set up using the Nernst-Planck application mode in the Chemical Engineering Module of COMSOL. The Moving Mesh (ALE) application mode keeps track of the deformation of the mesh.

3.2.3 Moving Boundary

The normal of the cathode is given moving mesh conditions so that there is adaptive mesh refinement and movement as the nanowire grows. The rate at which the mesh moves locally is calculated from the amount of material being deposited locally.

3.3 Results and Discussion

3.3.1 Chronoamperometry

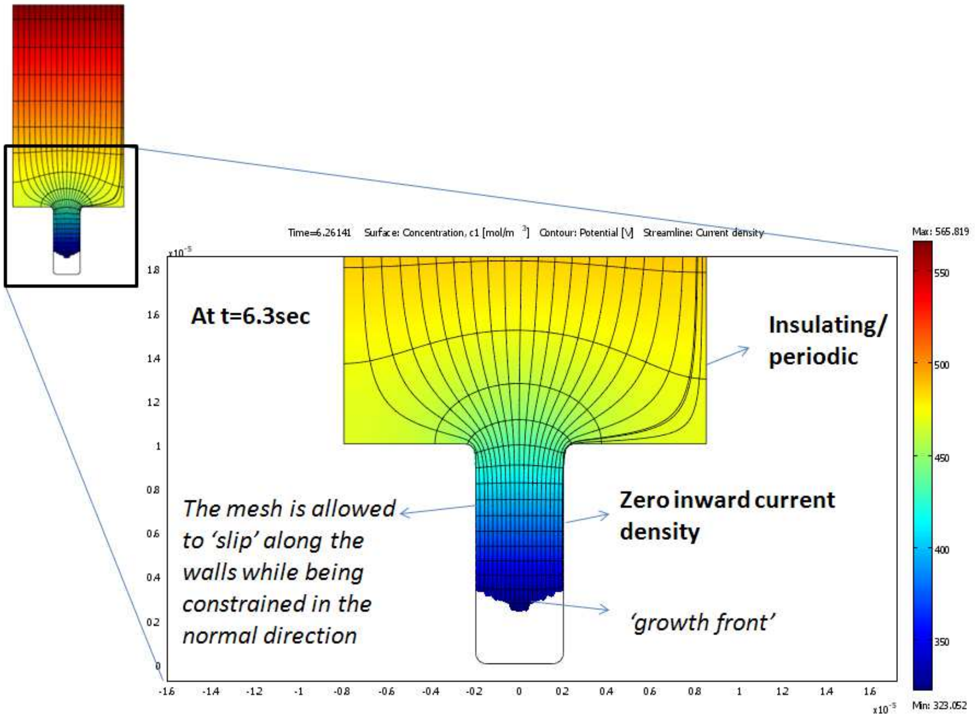

Fig. 3.3: Simulation of nanowire growth. Snapshot of growth after 6.3 seconds.

Fig. 3 shows a snapshot of growth after 6.3 seconds of growth. The anode potential is 0.08V while that of the cathode is held constant at -0.08V, and the solution is 0.5M $CuSO_4$ concentration to begin with. Top left of Fig. 3 shows a 'unit cell' of the microelectrode array. The streamlines represent current density, while the contour lines represent potential lines (concentration contour lines would look identical to potential contour lines). Furthermore, the various boundary conditions are shown.

The growing nanowire is depicted by the white region. It can be seen that the ‘growth front’ is not planar. This is because the current density is larger at the edges where the cathode and the insulating boundaries meet at 180° angle (This result/observation was confirmed by many other students during their presentations). The resulting uneven growth results in a characteristic shape of the growth front.

Furthermore, the potential contours are parallel in two regions: one, within the pores and two, in the bulk, while they curve in an arc (and so do the concentration contours, as will be seen later) as they exit the pores. As one would expect, the potential and concentration contours always end normal to the insulating boundaries. Also can be seen, from the rainbow coloring scheme, is that the concentration is depleted within the pores as the nanowire grows while it is enriched at regions closer to the anode. The current streamlines are perpendicular to the potential and concentration contours, as they should be.

In order to study the effect of geometry, simulations were carried on various geometries shown earlier (Fig. 1). Below, Fig. 4 shows a series of snapshots taken during the chronoamperometric electrodeposition of Cu into these various micropores. As can be seen, the diffusion clouds exit the shortest pore (top panel) the quickest and already overlap with the adjacent pores at 0.49s. On the other hand, the deeper pores (second panel) take about 1.2s (not shown) before the diffusion clouds overlap. As one would expect, in the third panel where the pores are as deep as the second panel but now has smaller interpore distance, the diffusion clouds overlap around 1.01s (not shown), that is, quicker than the second panel. This is expected because of the increased competition from nearby pores in the third case.

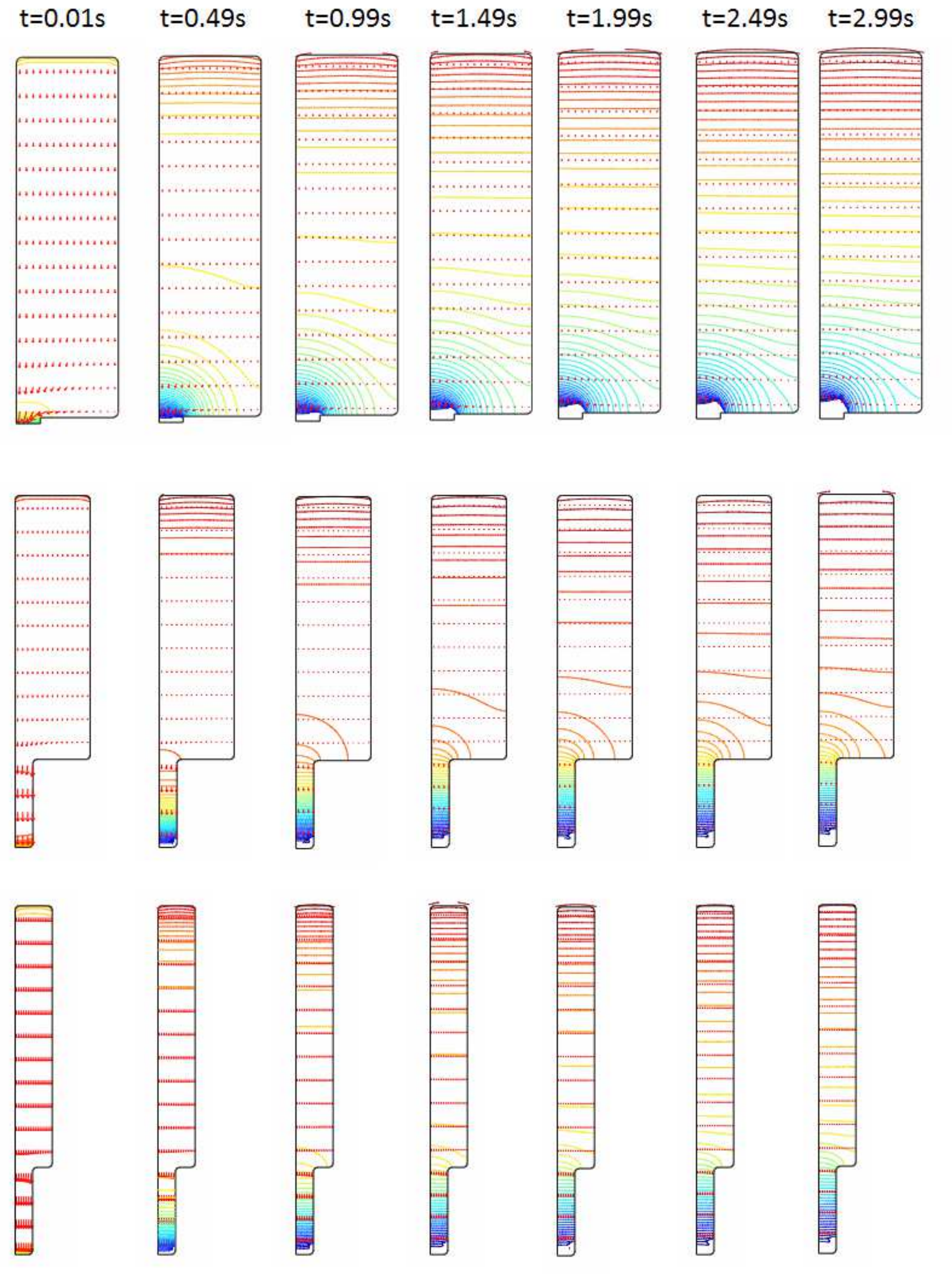

Fig. 3.4: Chronoamperometry. Electrodeposition inside pores of various lengths and interpore separations. The contour lines as well as the color scheme represent concentration of copper ions.

3.3.2 Current vs time for three different pores

Fig. 5 shows a plot of current (that is, the instantaneous current density integrated over the instantaneous cathode boundary) as a function of time for three different pore lengths (and having the same interpore spacing). The steady state current achieved is smaller for the deeper pores and increases for decreasing pore length. In particular, for the shortest pore length, the diffusion clouds exit the pore in 0.12s, resulting in a radial diffusion. This results in an increased mass transfer rate and thus large current densities for this case.

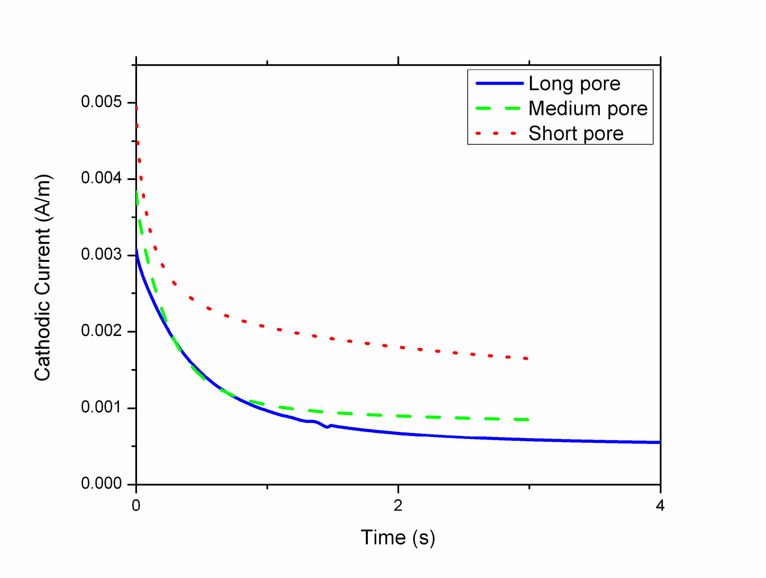

Fig.3. 5: Current versus time for various geometries.

3.3.3 Concentration vs time for three different pores

Fig. 6 shows the Cu^{+2} (and therefore that of SO_4^{-2}) ion concentration as a function of time for the various geometries. It can be seen that the medium length pore is depleted of Cu+2 ions the quickest at the cathode.

For the same pore length, it can be observed that shorter interpore spacing results is slower depletion of the Cu^{+2} ion at the cathode. This can be understood based again on the idea that with smaller interpore spacing, there is stiff competition from adjacent pores for the Cu^{+2} ions. In other words, the diffusion clouds overlap quickly for short interpore spacing, as was seen in Fig. 5 earlier, and thus results in radial diffusion, which in turn results in faster mass transfer of Cu^{+2} ions. Hence short interpore spacing will have a larger concentration of ions at the cathode.

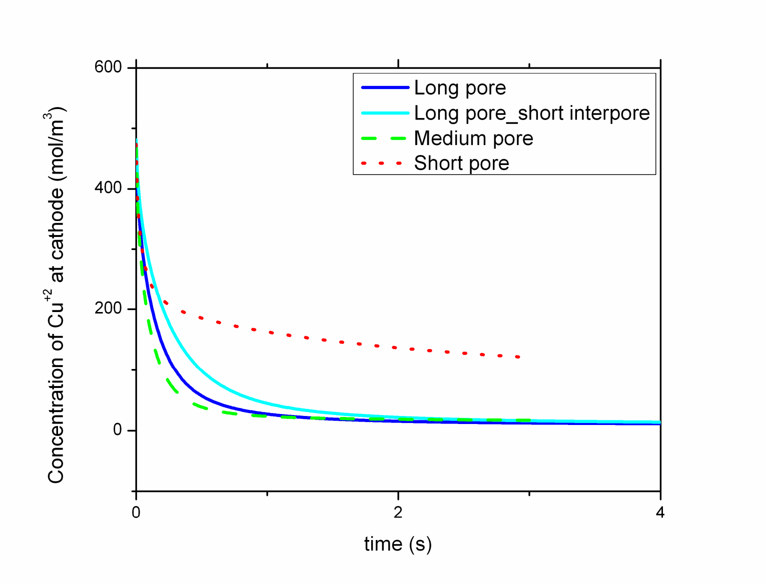

Fig. 3.6: Concentration of Cu^{+2} ions at the cathode versus time.

3.3.4 Variation of potential and concentration within the solution during Chronoamperometry

Figures 7 through 9 show potential at steady state as a function of distance from pore bottom (cathode) for the three different pore lengths. The cathode is at -0.08V while the anode is at +0.08V. It can be seen that longer pores have smaller ohmic potential drop in the solution while most of the potential drop occurs within the pores.

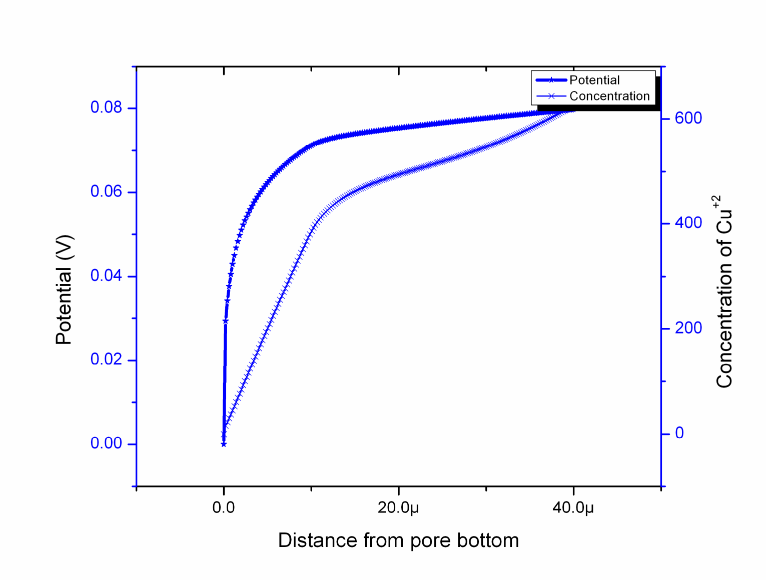

Fig.3. 7: Long Pore - Variation of potential and concentration as a function of distance from pore bottom.

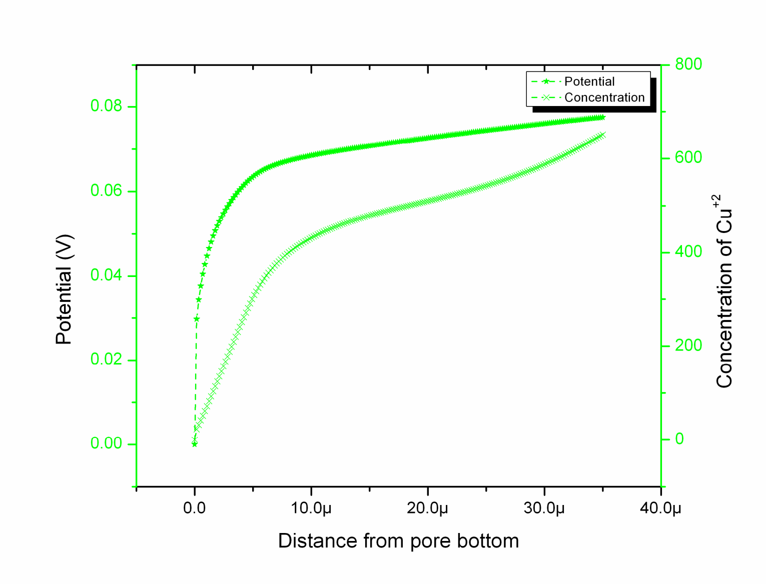

Fig.3. 8: Medium Pore - Variation of potential and concentration as a function of distance from pore bottom.

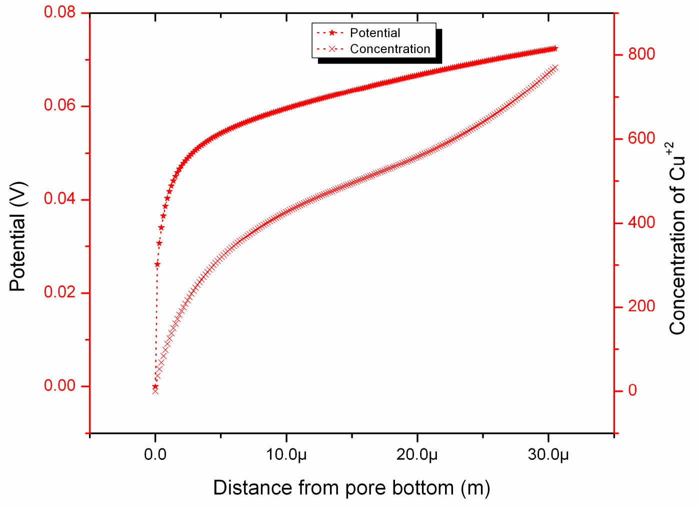

Fig. 3.9: Medium Pore - Variation of potential and concentration as a function of distance from pore bottom.

3.3.5 Cyclic Voltammetry (CV)

Current (A/m) vs potential (V) Cyclic Voltammetry curves for long, medium and short pores are shown in Fig. 10. While the potential of anode is again maintained at a constant value of +0.08V, the cathode potential is ramped at a rate of 100mV/s from 0V to -0.15V and then back to 0V (for the long pore, it was ramped to -0.2V and then back to 0V).

The current plotted is obtained by the integration of instantaneous current density over the instantaneous cathodic boundary, that is the integration is carried taking into consideration that this boundary is varying in shape and size as the nanowire grows during the CV scan.

A characteristic well-shaped CV plot is obtained during the forward scan, with a shallower curve obtained on the reverse scan. These results closely match those obtained in Ref. [1].It was observed that the reverse scan shallow curve is entirely an artifact of the geometry: it is an indication of the 'communication' between the anode and cathode. That is, the anode is not infinitely far away from the cathode, and is acting as a source of Cu^{+2} ions for the cathode. If the anode was brought closer to the cathode, then the reverse scan would overlap with the forward scan.

This could be resolved by either modifying the geometry to have even larger anode-cathode separation, or simply by decreasing the diffusivity of Cu^{+2} and SO^{-4} ions smaller. The former resulted in too many mesh points and thus caused memory issues for the solver, so the latter approach was adopted which was successful. A diffusivity of $2x10^{-5}$ cm^2/s was used in all the simulations for the geometries considered.

Furthermore, one can see that the long pore length shows an enhanced CV curve compared to the medium length pore, as was observed by [2-4]. This is because the diffusion clouds exit the medium pore quickly, while it takes much longer in the case of long pore lengths. Thus for the long pores, the diffusion is linear resulting in an enhanced peak even as the overall current density levels are smaller than the medium length pore case.

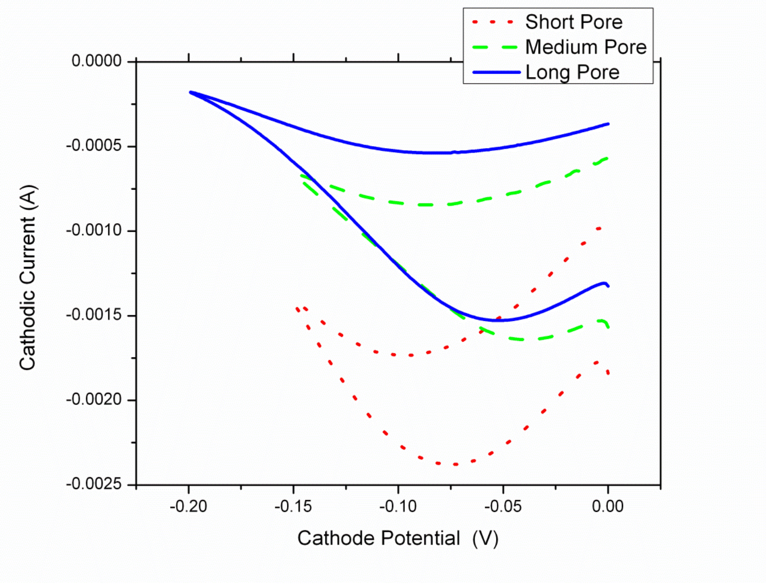

Fig. 3.10: Cyclic Voltammetry - current versus potential.

It can also be seen that the shortest pore results in the largest current density levels for the CV scans. In this case, the diffusion clouds exit the pore in 0.12s. Thus the diffusion changes from a planar diffusion to radial diffusion, which results in such large current densities [2].

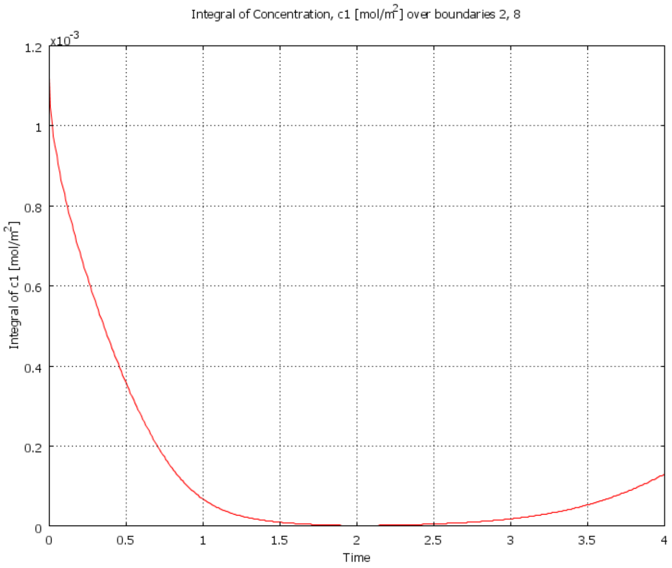

Fig. 3.11: Cyclic Voltammetry - Concentration of Cu^{+2} ions at the cathode versus time (potential being ramped @100mV/s from 0V to -0.2V (when t=2s) and then back to 0V (t=4s).

Concentration vs potential

Fig. 12 shows the concentration of Cu^{+2} ions at the cathode as a function of applied external potential during the CV scan for the three different cases. It can be seen that the long and medium pores are depleted of Cu^{+2} ions quickly than the short pores. This is because the more further the anode is from the cathode, as in the case of long pores, the longer the Cu+2 ions have to diffuse from the anode to replenish the diffusion layer at the cathode. This results in a quick growth of the diffusion layer for the long and medium pores.

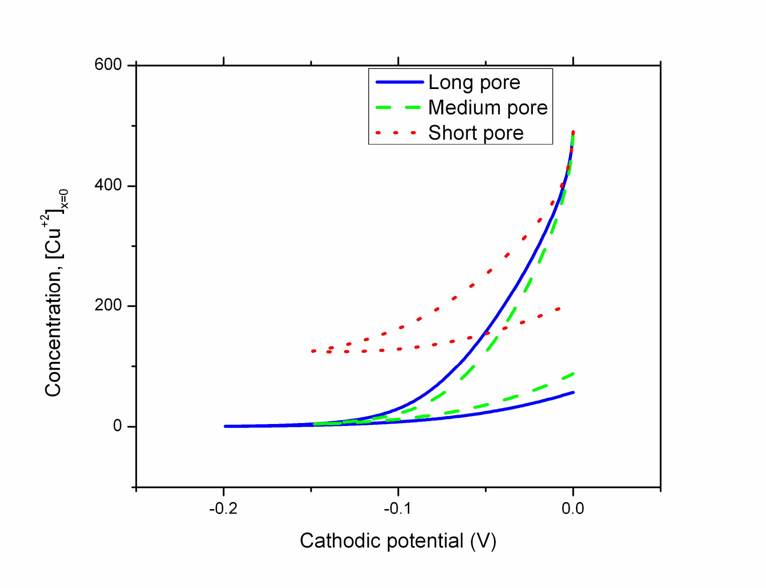

Fig. 3.12: Cyclic Voltammetry - concentration versus potential for various geometries considered.

3.4 Discussion and Summary

3.4.1 Electrodeposition of Nanotubes at high overpotentials

The geometry chosen in Fig. 1 and Fig. 2 is not entirely far from reality. When a metal contact is sputtered on one side of a free-standing anodized aluminum oxide (AAO) template, there is an unintended metal deposition within the pores which coats the pore walls upto a distance roughly equivalent to the diameter of the pores. When the AAO was etched off, metallic nanotubes remained (see SEM image in Fig. 13). A similar result was also obtained by Dickey et al [5].

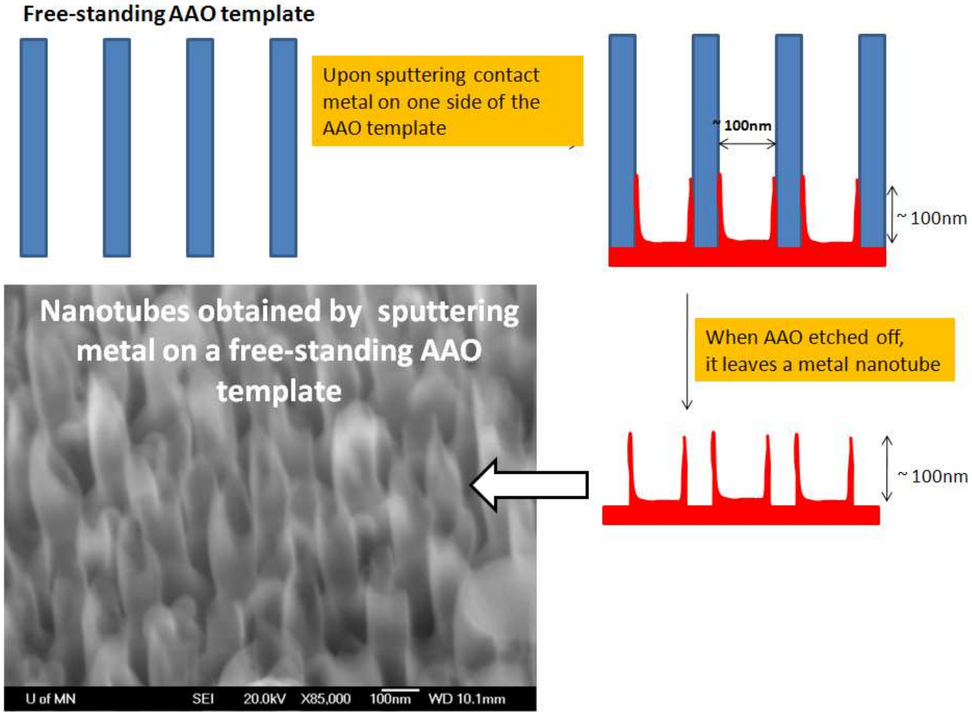

Fig. 3.13: Contact deposition on AAO templates leading to a tubular contact.

Furthermore, the fact that the current distribution is large at the edges was observed in [6], and was employed successfully to grow nanotubes. It was observed in [6] that under high current density conditions, there was predominant growth along the pore walls leading to nanotubes, whereas at low current density conditions, there was a uniform solid nanowire growth. These two growth conditions were used sequentially to electrodeposit core-shell nanowires in AAO-templates, the outer core electrodeposited at high current densities and the inner core under low current densities.

3.4.2 Bimodal Nanowire Growths

As a diffusion cloud exits a nanopore, it grows until it overlaps with the adjacent ones, depending on how quickly they are emerging out of the adjacent pores. This results in a non-uniform concentration distribution just outside the pores, and thus a tertiary current distribution ensues, leading to a multimodal nanowire growth. Fig. 14 shows an SEM image of one such multimodal nanowire growth obtained as part of the author’s research. It shows a cross-sectional image of Fe-Ga nanowires (which were grown in an AAO template followed by AAO being etched off completely leaving just the nanowires). It can be seen that towards the right of the image, the nanowires are of almost uniform length. However, there is a gradual transition to bimodal (or multimodal) distribution in the nanowire lengths as one goes towards the left of the image (which actually happens to be the center of the sample). This multimodal length distribution is clearly a result of tertiary current distribution. The author hypothesizes that because of the presence of a very large insulating packaging (not shown) present at the edges of the sample during growth (right side in the SEM image), the solution might have not been stirred properly there, resulting in a planar diffusion layer there. However, at the center of the sample, the vigorous stirring of the bulk keeps replenishing the pore openings, stopping the spherical diffusion clouds from merging into a planar diffusion layer. Thus one expects a tertiary current distribution at these regions, while at the right side, since the electrode is 'uniformly accessible', the distribution is more of a secondary current distribution.

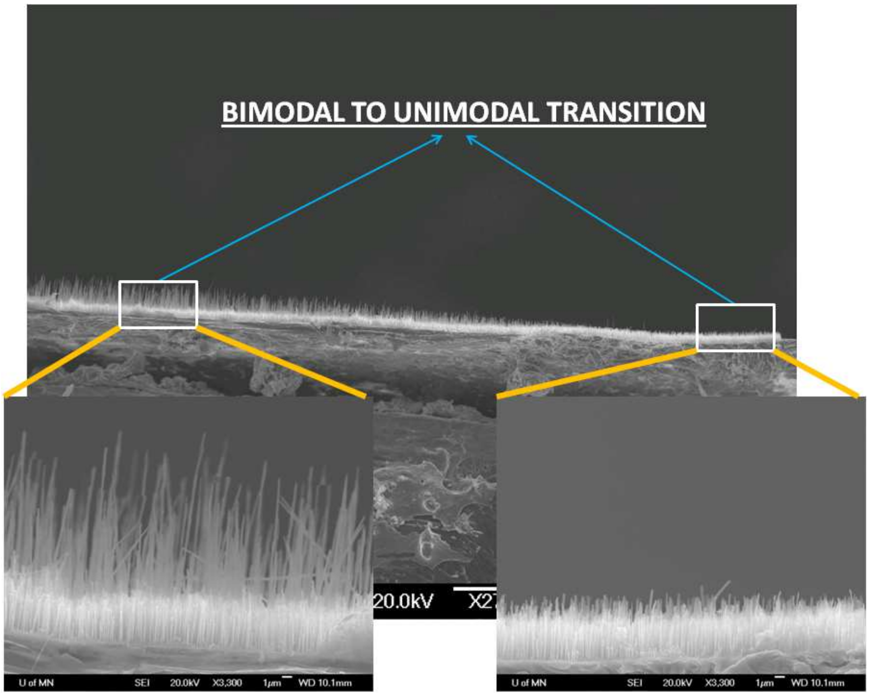

Fig. 3.14: Bimodal growth observed during the electrodeposition of FeGa alloy nanowires.

3.5 Summary

In summary, one can note that among the most important factors that decide the current and potential distributions over an electrode are:

1. geometry of the system
2. the conductivity of the solution
3. the activation overpotential (which depends on the kinetics of the electrode reactions)

4. the concentration overpotential (which is caused by the concentration differences between the electrode-solution interface and the bulk solution)

We can expect to have *primary current distribution* when the activation and concentration overpotentials are low, that is there are no appreciable concentration gradients inside the solution and the electrode reactions are kinetically fast. We can expect *secondary current distribution* when the electrode kinetics are slow, but the diffusion rate is very fast. The third case, *tertiary current distribution* occurs when the diffusion layer thickness is of the same order of magnitude as the characteristic length of the geometry of the electrodes. While convection only affects the region outside the hydrodynamic layer, the flux distribution within the diffusion layer is now dominantly defined by diffusion only, and hence the current distribution is entirely dependent on the shape and size of the diffusion layer in case of tertiary current distributions.

Thus, long nanowires are favored from the view point of diffusion because they are more accessible to diffusion than the shorter ones and therefore the local current density is larger there. That is, any difference in lengths of nanowires present either before or during the growth will only exacerbate as the growth progresses in tertiary current distribution mode. This clearly explains the multimodal growth observed in the growth of kinetically slow Fe-Ga electrodeposition (Fig. 14).

In fact, at limiting current conditions, the situation is similar to primary current distribution because Ficks second law for the steady state is formally identical with the Laplace law, and the boundary conditions are also the same ($c_{(x=0)} = 0$ = constant at the limiting current; φ_e = const in primary distribution) [7]. Thus, in tertiary current distribution, geometry plays a very important role if not the dominant role.

CHAPTER 4: OPTIMIZATION OF NANOWIRE GROWTHS

Electrochemical fabrication of large-area, high-density arrays of high-aspect ratio ferromagnetic nanowire structures has been the focus of vigorous research owing to the potential for applications in technologically critical areas like ultrahigh density magnetic memory,[1-5] spintronics and novel magnetic-sensors,[6-10] and biological applications.[11,12] There is also tremendous potential to use magnetostrictive nanowires as functional elements in advanced nanoscale sensors and actuators.[13,14] Recently, it has been theoretically predicted that the high surface-stresses present at the nanoscale induce high internal compressive stresses, which in turn result in a shape memory effect in Cu nanowires.[15] These compressive preloads are also likely to enhance magnetostriction in ferromagnetic nanowires similar to bulk magnetostrictive materials which are typically mechanically biased with a compressive preload in normal operation.[16] Among the known magnetostrictive alloys, very few show as high a magnetostriction as do the giant magnetostrictive alloys Terfenol-D ($Tb_xDy_{1-x}Fe_2$)[17] and Galfenol ($Fe_{1-x}Ga_x$).[16,18] Galfenol is a superior engineering material compared to Terfenol-D because of its higher ductility and strength.[18] In addition, bulk crystalline $Fe_{81}Ga_{19}$ alloys are reported to have magnetostrictive constants exceeding 400 ppm at room temperature[19] (as opposed to 30 - 130 ppm for bulk Fe, Co, Ni based alloys[20]). Electrochemically deposited Fe-Ga nanowires have been demonstrated to have excellent flexibility,[21] thus promising a high magneto-mechanical coupling with potential applications as sensing elements in a variety of microelectromechanical (MEMS) and nanoelectromechanical (NEMS)-based biomimetic devices.[22,23]

4.1 Non-Uniformities in Electrodeposited Nanowire Lengths

Electrodeposition of Fe-Ga nanowire arrays has been reported earlier,[24-27] with homogeneous alloy compositions being achieved throughout the array. However, unwanted hydrogen evolution reactions and oxide formations[28] result in serious non-uniformities in nanowire lengths, the mention of which is rare in the literature.[29] In this work, we overcome these issues by controlling mass-transfer and hydrodynamic conditions using a novel modified (rotating disk electrode) RDE-template. This controlled electrodeposition of Fe-Ga nanowires will also benefit a broad spectrum of researchers studying the possibility of synthesizing at nanoscales the gallium-based shape memory alloys like those of CoNiGa,[30] NiFeGa[31] and NiMnGa.[32] Magnetic properties of continuous ferromagnetic nanowires[33-39] as well as those of various ferromagnet/non-magnet (Co/Cu, NiFe/Cu, NiFe/Au, Ni/Cu, CoNi/Cu) multilayered nanowire arrays have been reported earlier.[40-45]

4.2 Experimental Conditions

Sample preparation: Commercially obtained (Synkera) Anodized Aluminum Oxide (AAO) templates of 100 nm nominal diameters were used as templates for electrochemical deposition of the Fe-Ga and Fe-Ga/Cu nanowires. The templates were sputter-coated with a thin adhesion layer of Ti followed by a thicker Au coating. These templates were then annealed at 200°C in ambient air in order to improve the contact. The template was directly contacted to the rotator using Indium, followed by insulation using Xtal Bond, and rotated at a speed of 1800 rpm during electrodeposition.

Electrodeposition conditions: The electrolyte consisted of $FeSO_4$ (15 mM), $Ga_2(SO_4)_3$ (35 mM) and Na_3-citrate (35 mM) in DI water. pH was adjusted to 3.75 with diluted NaOH. The counter electrode for all the electrodeposition experiments was a thin sheet of platinum foil. Deposition potential of -1.12 V vs. Ag/AgCl was used for Fe-Ga electrodeposition. During pulse deposition (Figure 1d), a rest potential of -0.8 V was used so that Fe-Ga did not strip off during the rest pulse. For Fe-Ga/Cu multilayered deposition, $CuSO_4$ (1.5 mM) was added to the above solution. Deposition potentials of -1.12 V and -0.8 V vs. Ag/AgCl were used for Fe-Ga and Cu electrodeposition, respectively. The optimized deposition conditions resulted in compositions close to $Fe_{80}Ga_{20}$, as characterized by SEM-EDS. In multilayered nanowires, Cu co-deposited during the deposition of Fe-Ga layer, but the ratio of Fe:Ga was found to be still 80:20.

Methods: The rotating disk electrode was obtained from Gamry Instruments, and was capable of rotating to speeds up to 10000 rpm. XRD analysis was done on the samples after polishing off the Ti/Au contact, using Bruker-AXS microdiffractometer with 2.2kW sealed Cu x-ray source. VSM was done at room temperature using an automated vector VSM from LakeShore with applied fields upto 1 T. SEM and EBSD were performed using a JEOL 6500 scanning electron microscopy, equipped with an Orientation Imaging Microscopy (OIM) and EBSD detector (EDAX TSL). EBSD measurements were done using the following parameters: tilt of 70°, accelerating voltage of 20 kV, spot size of less than 10 nm and a measurement step size of 30 nm. BCC α-Fe phase was used for indexing, according to the TSL OIM Analysis 5.1 database.

4.3 Optimization of Nanowire Growths

Non-uniform growth fronts are a particular problem in the case of alloy nanowires involving non-ideal metals (e.g., Bi_2Te_3,[46] Fe-Ga[24]). A typical array of Fe-Ga nanowires grown by standard electrochemistry is shown in Figure 1.

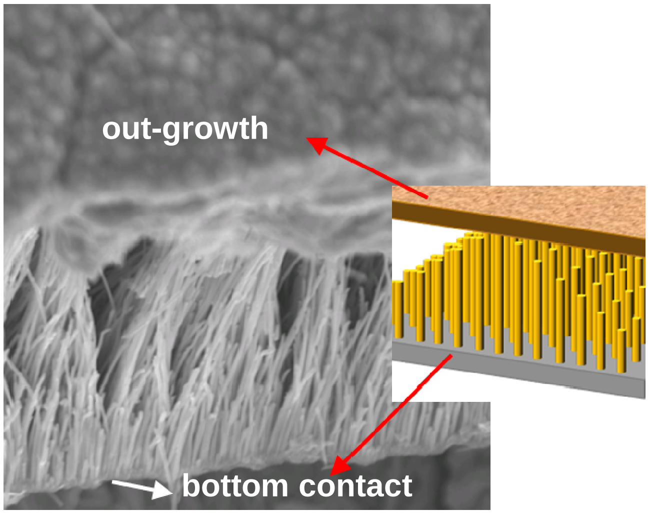

Fig. 4.1. Severe non-uniformities in nanowire lengths are typically observed in electrodeposition of alloys involving non-ideal metals. Wherever the nanowires reach the top of the pores, there is preferential out-growth which blocks the adjacent pores. The result is a characteristic 'roof' on top of the nanowires.

A commercial template with large non-idealities in interpore spacings was used while the electrolyte was agitated with a laboratory magnetic stirrer. It can be seen that some of the nanowires grew much faster than their neighboring ones. Once these nanowires reached the top of the pores, they formed a metal cap blocking the growth of the adjacent pores. Plausible reasons for the non-uniform growth rates are: non-idealities in interpore spacings in commercial templates, non-uniformities in the mass-transfer and nucleation rates from pore-to-pore, hydrogen gas evolution blocking some of the pores etc. In Bi_2Te_3 nanowire arrays, the non-uniform growth front issue was only recently resolved using a low temperature pulse deposition method while employing highly ordered AAO templates specifically made for the purpose of improving mass-transfer.[46] However, it would be commercially advantageous if one does not have to be constrained by these restrictions.

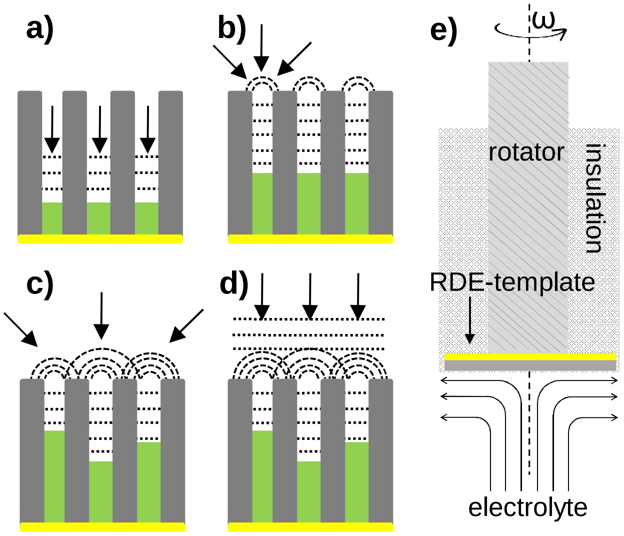

Fig. 4.2. Time evolution of diffusion fields during electrodeposition in nanoporous templates. a) During initial stages of growth, linear diffusion fields lie entirely within the pores, b) as deposition proceeds, the radial diffusion fields just emerge out of the pores, c) subsequently, there is uneven overlapping of the radial diffusion fields, d) finally, extensive overlapping results in linear diffusion fields outside the template, e) in-house modified rotating disk electrode (pores facing down into electrolyte) that was used to controllably vary mass-transfer conditions from those shown in b) to d) above. The streamlines in the electrolyte near the RDE-template surface are illustrated.

To overcome this barrier, we need to understand the fundamentals of mass-transfer occurring during electrodeposition in AAO templates. It is well known that electrodeposition in nanoporous templates occurs in a series of steps during which the depletion zone (Nernst layer) grows with time as deposition proceeds **(Figure 2)**. In the initial stages, linear diffusion occurs within the pores (Figure 2a). When the depletion layer grows longer than the pore length, radial diffusion fields envelope the pore openings (Figure 2b). With time, these radial diffusion fields merge with each other (Figure 2c), and eventually extensive overlap results in linear diffusion fields again (Figure 2d). While this phenomena has been studied earlier, there has been no clear effort in reporting what effect each of the above mentioned diffusion fields have on the growth quality.

Experimentally, radial diffusion (Figures 2b and 2c) determines the overall electrodeposition process. Hence, any non-uniformities present in the overlapping diffusion fields are likely to reflect in the nanowire growth-fronts, and therefore the nanowire lengths. In practice, the non-idealities present in the templates as well as non-simultaneous nucleation exacerbate the non-uniformities even further. In this study, these issues were tackled sequentially. First, in order to create uniform hydrodynamic conditions near the template surface, a modified (rotating disk electrode) RDE-template capable of rotating at high speeds was employed (Figure 2e). Rotation of the RDE-template causes the nearby solution to be drawn towards the electrode surface, as represented by the streamlines, thus enabling a controllable laminar flow as a function of rotation rate. The solution within the pores remains unstirred; however by increasing the rotation rate sufficiently, it is possible to greatly minimize the uneven overlapping of the radial diffusion layers of Figure 2c.

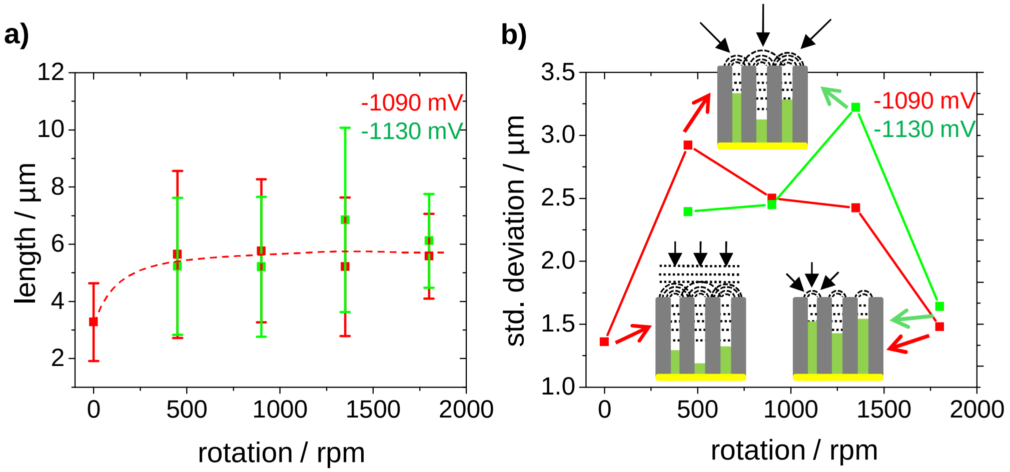

Fig. 4.3. Variation of a) mean nanowire lengths and b) standard deviations in nanowire lengths as a function of rotation of the RDE-template for two different potentials. The cartoons illustrate the mass-transfer conditions existing at the corresponding rotation rate. Both high and low rotation rates resulted in a narrow distribution in nanowire lengths, but the decreased mass-transfer in the latter resulted in very slow growth rates. Intermediate rotation rates surprisingly resulted in widened nanowire length distributions, attributed to non-uniform overlapping of diffusion fields. Identical experimental conditions (electrolyte composition and deposition time) were used for all samples. Potentials are with respect to standard calomel electrode (SCE).

Figure 3 shows the effect of rotation rate on the nanowire lengths and the nanowire length distributions, as a function of deposition potential. The data was obtained by performing a statistical analysis on nanowire lengths from cross-sectional SEM images of each sample (as shown next in Figure 4). It can be seen in Figure 3a that the nanowire lengths almost double when the rotation rate is increased to above 900 rpm as compared to no rotation (0 rpm). A plot of the standard deviations as a function of rotation (Figure 3b) revealed an interesting phenomenon: the presence of a maximum at intermediate rotation rates. This maximum occurred at a lower rotation rate when the deposition potential was lowered from -1.13 V to -1.09 V. In an unstirred solution (0 rpm in Figure 3b), extensive overlap of radial diffusion fields resulted in linear diffusion profiles outside the pores. Thus, the non-uniformity was minimized, but only at the cost of the growth rate, as can be seen in the small nanowire length for 0 rpm in Figure 3a. High rotation rates of 1800 rpm (Figure 3b) minimized the overlap of radial diffusion fields, resulting again in a narrowed distribution in nanowire lengths. The increased mass transport at 1800 rpm also increased the nanowire lengths (Figure 3a). At intermediate rotation rates, the enhanced mass-transfer rate decreased the diffusion layer thickness, but was not enough to completely eliminate the overlapping of the radial diffusion profiles. This resulted in severe non-uniformities in mass transfer rates from pore-pore, observed as a maximum in the standard deviations in Figure 3b.

Figure 4a shows SEM image obtained during a typical Fe-Ga nanowire growth, under commonly employed conditions of agitation with a magnetic stirrer. A statistical analysis (superimposed) showed a bimodal distribution in the nanowire lengths, with an overall relative standard deviation of 75%. The shorter nanowires were not only abundant, but their distribution in lengths was narrower than the larger wires. However, with the use of the RDE-template at a rotation rate of 1800 rpm (Figure 4b), not only was the bimodal distribution eliminated, but the relative standard deviation was reduced to 27%. This wide distribution seen in Figure 4b may have been caused by non-simultaneous nucleation at the bottom of the pores. To help facilitate a simultaneous nucleation, 200 nm of a noble metal Cu was first electrodeposited in the pores to act as nucleation sites for subsequent Fe-Ga deposition. This resulted in a greatly improved uniformity (Figure 4c). Further improvement was realized when pulse deposition was employed, in addition to the use of RDE-template and Cu seed layer. Fe-Ga deposition pulse was applied for 1 s, followed by a 2 s ‘rest’ period. The rest period ensured that the nanowire growth always occurred in the linear diffusion regime (Figure 2a). As a result, non-uniform overlapping of diffusion fields was completely avoided, and resulted in very uniform nanowires with just 3% relative standard deviation (Figure 4d). Thus, by understanding the various aspects of mass-transfer, we were able to completely eliminate the bimodal distribution in nanowire lengths and fabricate nanowire arrays with greatly enhanced repeatability and uniformity in lengths over the whole area of the template.

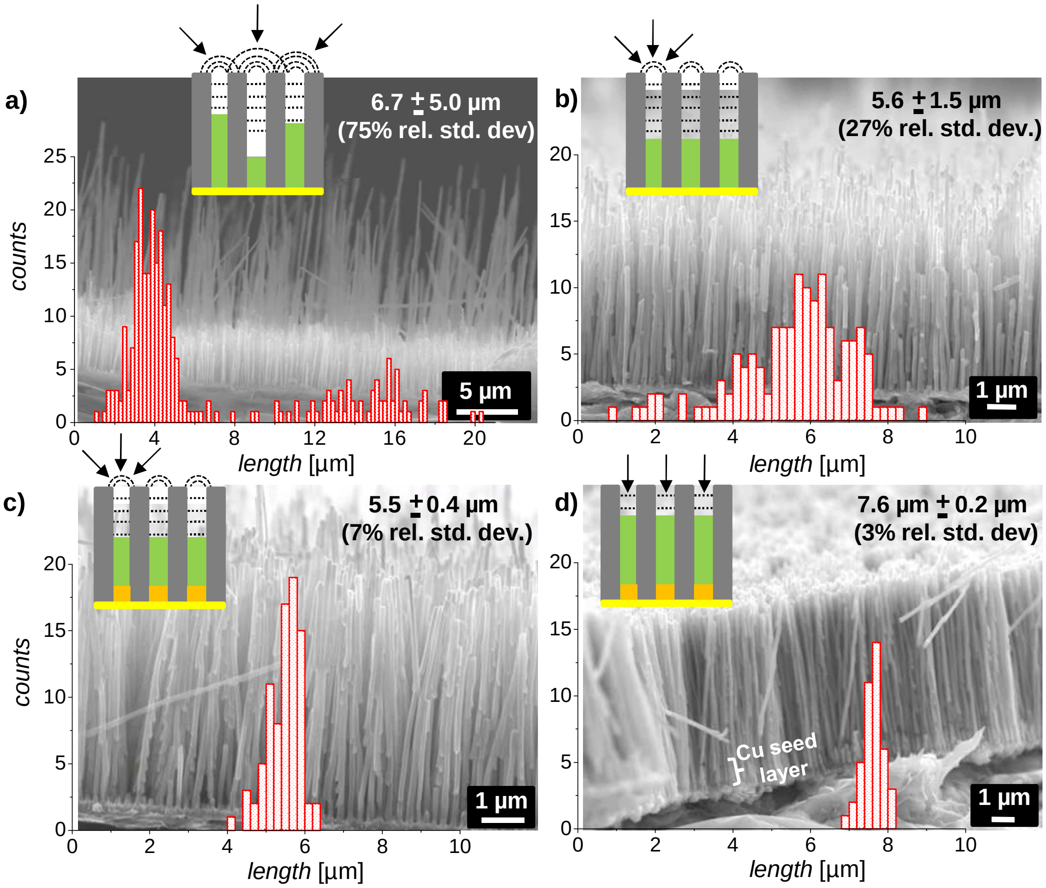

Fig. 4.4. Optimization of Fe-Ga nanowire growths. Statistical analysis of nanowire lengths is superimposed on the corresponding SEM image, and the schematics represent the diffusion

profiles existing during growth in each case. a) a bimodal distribution was obtained when the solution was agitated using a magnetic stirrer, b) after use of RDE-template at a rotation rate of 1800 rpm, c) after use of Cu seed layer in addition to RDE-template and d) use of pulse deposition in addition to Cu seed layer and RDE-template. Identical growth conditions including deposition potential, solution concentrations and time of deposition were used.

We were then able to fabricate Fe-Ga/Cu multilayered nanowire arrays of various structures (see **Figure 5a**) with enhanced reproducibility and uniformity in segment thicknesses over the whole area of the template. Structure A represents one extreme with the largest Fe-Ga thickness and zero Cu thickness, and structure E represents the other extreme with the smallest Fe-Ga thickness and largest Cu thickness.

4.4 Structural Characterization

Figure 5b shows XRD characterization done on structures A and B. The XRD patterns for Fe-Ga were indexed based on disordered body-centered-cubic α-Fe (or *A2*) phase, in which the gallium atoms randomly substitute the iron atomic positions. Incorporation of Ga atoms caused an increase in lattice parameter from that of Fe, as can be seen from a shift of Fe-Ga peaks to lower 2θ values when compared to JCPDS Fe peaks. Both A and B had a <110> preferred orientation for the Fe-Ga segments, in addition to some <211> and <200> oriented grains. On the other hand, analysis of Cu peaks in structure B indicated a polycrystalline growth without any significant texture. This was expected for the strongly diffusion limited growth of Cu segments.[49] However, it was surprising that the polycrystalline Cu segments did not disrupt the (110) texture of Fe-Ga layers to the extent we expected. Most likely, the citrate ions present in the electrolytic bath not only acted as a complexing agent but also as a leveling agent. A similar conclusion was drawn in a previous study on electrochemical deposition of multilayered Ni/Cu thin films where it was found that the loss of texture of Ni layers was minimized when using a citrate-based electrolyte instead of the conventional sulfate and sulfamate baths.[49]

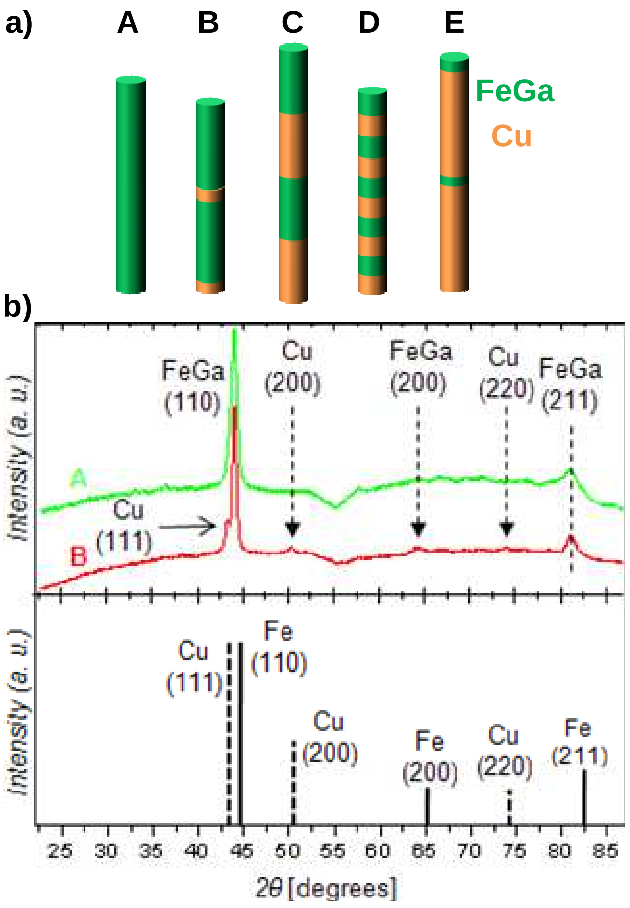

Fig. 4.5. a) 100 nm diameter structures studied in this work. A: [> 25 AR^{FeGa}*], B: [4.0 AR*^{FeGa}* / 0.5 AR*^{Cu}*]*$_{29}$*, C: [3.0 AR*^{FeGa}* / 3.0 ARCu]*$_{8}$*, D: [1.0 AR*^{FeGa}* / 1.0 ARCu]*$_{15}$*, E: [0.5 AR*^{FeGa}* / 5.0 ARCu]*$_{50}$*. AR = aspect ratio = length/diameter. The subscripts denote number of [Fe-Ga/Cu] bilayers. b) XRD patterns for structure A (Fe-Ga nanowires) and structure B (representative of the Fe-Ga/Cu multilayered nanowires). Nanowires were embedded within the AAO matrix. JCPDS data for Fe (#00-006-0696) and Cu (#00-004-0836) are shown in the bottom panel.*

Detailed microstructural analysis on structure A was done using TEM and EBSD **(Figure 6)**. The (high resolution) HRTEM image (Figure 6b) taken at an edge of the nanowire (Figure 6a) showed parallel atomic rows of these (110) planes. The $d_{(110)}$ interplanar spacing was calculated to be 0.2 nm, confirming XRD results. The SAED pattern (see inset) of this nanowire confirmed a crystalline electrodeposition, with <110> preferred orientation. EBSD analysis done on structure A is presented in Figures 6 c-e. Orientation imaging microscopy (OIM) enabled us to obtain (110) pole figure (PF) and inverse pole figure (IPF) images, and thereby the grain distribution and their orientations. The IPF image in Figure 6c

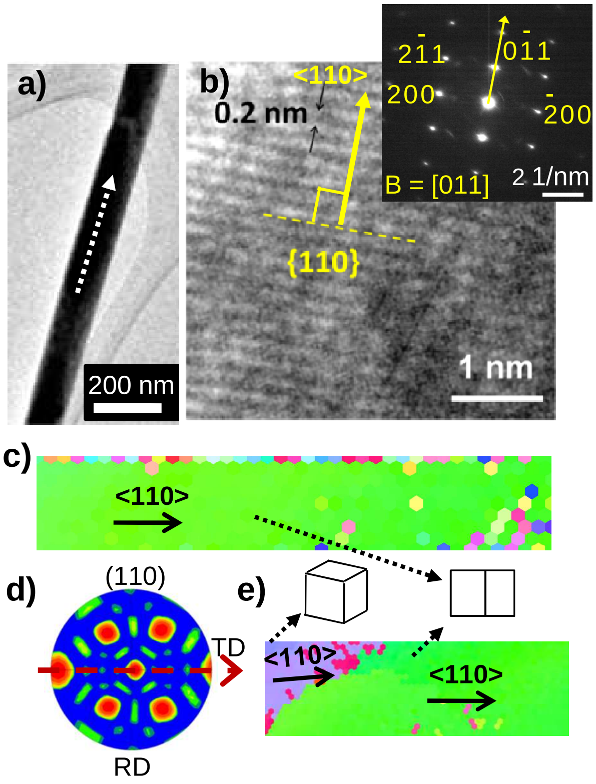

Fig. 4.6. Microstructure analysis of structure A. a) TEM image of nanowire. b) HRTEM image showing a crystalline growth. (inset) SAED pattern with arrow shown pointing along the nanowire axis. c) EBSD analysis showing Inverse pole figure (IPF). d) corresponding 110 pole figure. e) IPF of a different section of the same nanowire showing a low angle grain boundary defect.

shows a nanowire with <110> orientation along the longitudinal direction. The scatter along the upper edge of Figure 6c was caused by the curvature at the edge. The corresponding (110) pole figure (Figure 6d) clearly showed the crystalline nature of this segment of the nanowire. However, at another segment of the same nanowire, a low angle grain boundary was imaged (Figure 6e).

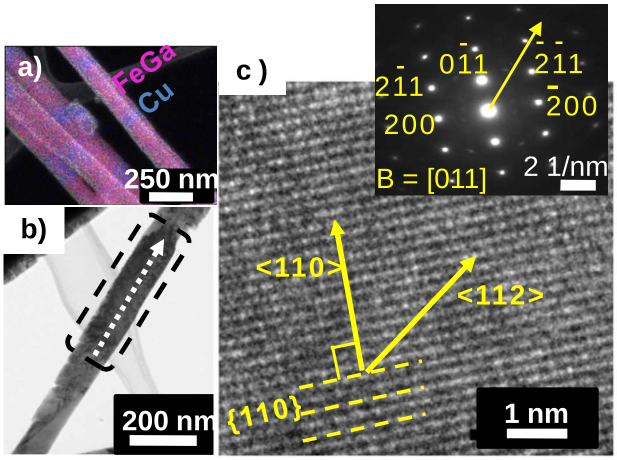

Fig. 4.7. Microstructure analysis of multilayered nanowires. a) SEM-EDS compositional map of [330 nm Fe-Ga] / [90 nm Cu] multilayered nanowires. b) TEM image showing Fe-Ga segment in a different nanowire. c) HRTEM image showing crystalline growth of Fe-Ga segment. (inset) SAED pattern of the Fe-Ga segment with arrow shown pointing along the nanowire axis. Corroborating XRD results, the TEM results showed the Fe-Ga segments in all structures had a preferential (110) texture along the nanowire length.

Fe-Ga/Cu multilayered nanowires were characterized in **Figure 7.** An SEM-EDS compositional map of Fe-Ga/Cu multilayered nanowires collected over a TEM grid show uniform Fe-Ga and Cu thicknesses. The leveling effect of the citrate electrolyte mentioned earlier was expected to smoothen interface irregularities by preferential electrodeposition into recesses,[49] and as expected relatively sharp interfaces were observed between the Fe-Ga and Cu segments (see Supporting Information).[50] Figure 7b shows the TEM image of a different multilayered nanowire (Fe-Ga segment is within dotted box). HRTEM image (Figure 7c) of the Fe-Ga segment showed a highly crystalline growth even in the multilayered nanowires, affirming the growth optimization enabled by the use of citrate baths. SAED pattern (inset of Figure 7c) of the Fe-Ga segment showed that the <110> direction was tilted away from the nanowire axis and the <112> direction was close to the nanowire axis. Based on XRD and EBSD results (Figure 5), Fe-Ga segments with this orientation were present to a small extent in all the nanowire structures. Furthermore, analysis of the reciprocal distances in SAED patterns showed that the (110) interplanar spacing in the multilayered nanowire was 4% larger than that in structure A, very likely due to codeposition of Cu within the Fe-Ga segments. Confirming XRD, TEM diffraction studies on Cu segments indicated a slight polycrystallinity.

4.5 Magnetic Characterization

The crystalline easy axis of bulk crystalline Fe-Ga alloys is along <100> direction, and the electrodeposited nanowires have a strong <110> texture along the nanowire axis, with randomized <100> orientation perpendicular to the axis. This randomization of crystalline easy axis results in negligible net magnetocrystalline anisotropy, so that the magnetic properties of the array are determined entirely by the competition between exchange energy, the demagnetization energy, and the Zeeman energy. Various modes of magnetic reversal in nanowires have been predicted theoretically (**Figure 8a**) including coherent rotation (CR), in which all the spins rotate coherently; transverse wall (T), in which moments invert progressively via propagation of a transverse domain wall (*localized* CR mode); curling (C), in which all the moments curl simultaneously; and the vortex wall (V), in which the moments invert progressively via propagation of a vortex domain wall (*localized* C mode).[34] The arrays reverse by whatever mode is energetically favorable and presents the smallest coercivity for that nanowire diameter and applied field angle.[37] Given this, it has been theoretically predicted that at low applied field angles, small diameter nanowires undergo reversal by T mode instead of CR mode,[34] whereas larger diameter nanowires undergo reversal by V mode instead of C mode.[38, 51] On the other hand, at applied field angles approaching 90°, CR mode presents the smallest coercivities.[34, 37] It is well known that the magnetization reversal of a nanowire array occurs by successive irreversible switching of individual nanowires.[36,38,52] However, owing to finite differences in nanowire lengths, surface defects, microstructure and mean magnetostatic fields from the array, there is a wide distribution in switching fields. Then, the macroscopic H_c values measured using VSM correspond to the configuration of zero magnetization of the whole array, that is, to the median of the switching field distribution. In addition, it was recently shown that even as inter-wire magnetostatic interactions modify the magnetic behavior of the array,[53] they do not significantly alter the magnetization reversal processes in the nanowires.[40] Therefore, parameters like M_r and H_c can be used as indicators of the various types of magnetization states at remanence and at coercive fields, and of the various magnetization reversal mechanisms.[35,36,40,54,55]

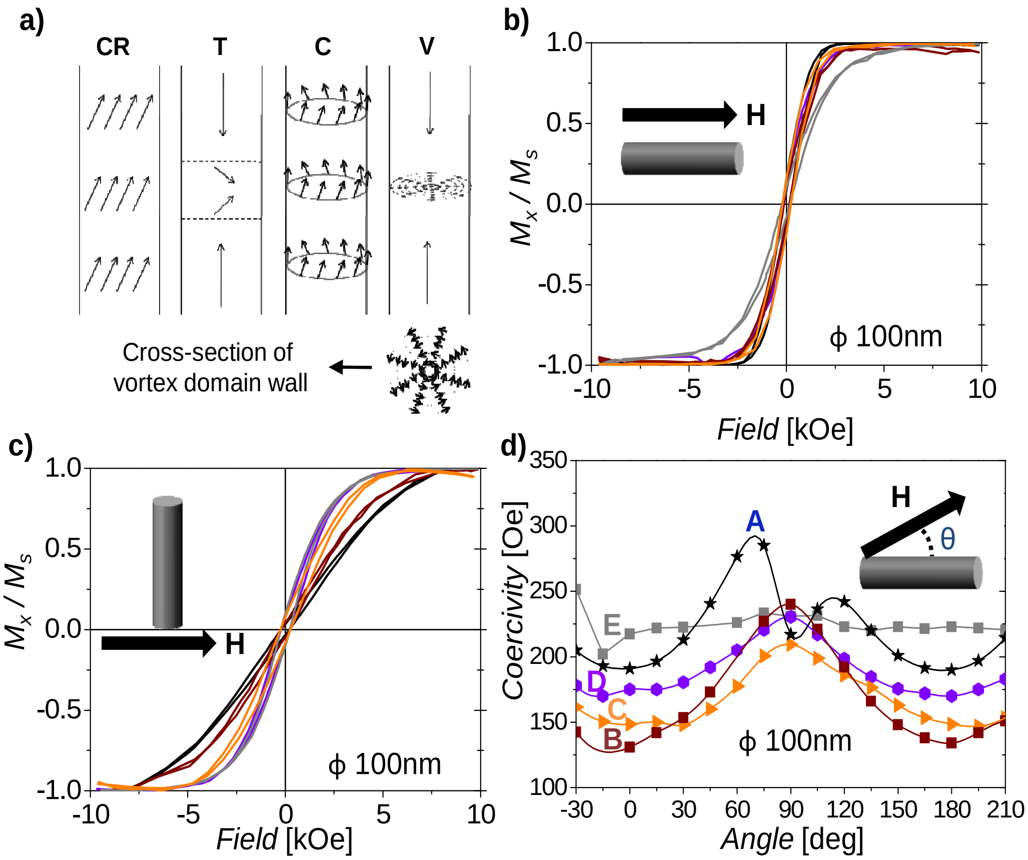

Fig. 4.8. a) Common modes of magnetization reversal in nanowires. CR: coherent rotation, T: transverse domain wall, C: curling and V: vortex domain wall. Here, the moments are shown reversing under the application of an external field applied in the downward direction. b) parallel and c) perpendicular hysteresis loops of structures A - E. d) Coercivity as a function of applied field angle for the various structures.

If future devices are to utilize the magnetostrictive property of Fe-Ga in nanowires, the designer has to be able to rotate the moments from along the nanowire axis to perpendicular to the axis (or reverse) so as to result in a length change. The feasibility of doing this was demonstrated in individual Fe-Ga/Cu multilayered nanowires in our earlier work.[56] Here, we study multiple Fe-Ga/Cu multilayered structures (Figure 8) by varying the aspect ratios of both Fe-Ga and Cu layers in order to elucidate on the balance between shape anisotropy and intra-wire magnetostatic interactions on the reversal mechanisms, and therefore on the measured coercivities. Parallel and perpendicular hysteresis loops (Figure 8b and 8c, respectively) indicated easy axes along the nanowire axes for all structures, except for structure E which was intentionally engineered to be isotropic.

H_c values measured as a function of angle are shown in Figure 8d. Theoretically, in nanowires undergoing reversal by either C or V modes, the coercivities increase with applied field angles, peaking at perpendicular (90°) fields.[37,38] On the other hand, for the CR mode, the coercivities decrease with applied field angles in the 0 - 90° angular range.[37] The system will experience reversal by the mechanism that has the lowest coercivity for that angle. As a result, the coercivities initially increase with applied field angle according to V mode, but there may exist a critical angle above which CR mode is favored after which coercivities decrease. In Figure 8d, structure A experienced this competition between the two modes. The H_c values initially increased indicating reversal by V mode in the low angular regime, but decreased at high angles indicating a contribution from CR mode reversal. This resulted in two distinct peaks at approx. 70° and 120° angles. In other words, with fields perpendicular to the nanowires, the reversal mode was a mixture involving a coherent rotation of moments *within* the nanowire and a reversal of vortex structures *at the ends* of the nanowires. These results are consistent with the in-field MFM study[38] of 60 nm diameter individual continuous Fe nanowires, where it was found that when negative fields were applied close to 0° angles, reversal took place by vortex domain wall propagation (V mode). However, at higher angles, a mixed mode of reversal set in: a coherent rotation of the magnetic moments inside the nanowire was observed while the magnetic moments at the ends of the nanowire formed into pinned anamorphic vortex structures.

The drop in H_c values observed for structure A (see Fig. 5) around 90° angle was absent for the multilayered structures B - E. In fact, the multilayered structures exhibited well defined bell-shaped curves that one would expect for a *pure* vortex/curling reversal mode.[37] That is, there was no contribution from CR mode, and reversal was completely dominated by V mode. This was expected because as the Fe-Ga aspect ratio decreased from 25 in structure A to 4 or less in the multilayered structures, the volume of moments undergoing CR mode reversal within each Fe-Ga segment decreased.

Furthermore, it is interesting to note that the H_c vs. θ curves of multilayered structures B - E appeared to converge at 90° applied field angles. To understand why, consider structure E in which the Fe-Ga aspect ratio was just 0.5, hence the volume of each Fe-Ga segment was expected to be composed mostly of pinned vortex structures present at either end. Therefore, the coercivity exhibited by this structure was solely determined by reversal of the pinned vortices. In addition, this structure E exhibited identical H_c values independent of applied field angle, indicating identical reversal mechanism for all applied field angles. Given that all the other multilayered structures (B - D) exhibited similar H_c values as structure E at 90°, it is very likely that the reversal of pinned vortex structures solely determined the 90° H_c values in them as well.

4.6 Conclusions

In this study, we have accurately controlled the electrodeposition of Fe-Ga/Cu multilayered nanowires by using novel modified RDE-templates together with Cu seed layers and pulsed deposition. The use of a citrate-based electrolytic bath enabled highly textured growth of Fe-Ga segments. Magnetic characterization revealed that in Fe-Ga/Cu multilayered nanowires, the coercivities depended on the aspect ratios, and on the applied field angles. At low applied field angles, the magnetization reversal occurred mainly by the nucleation and propagation of a vortex domain wall. At large applied field angles, a mixed mode of reversal set in, involving a coherent rotation of magnetic moments *within* the Fe-Ga segments and a reversal of vortex structures *at the ends* of the Fe-Ga segments. However, only the latter determined the H_c values at 90° applied field angles, except in structure A with very high Fe-Ga aspect ratio. Thus, we have demonstrated that by controlling the aspect ratios of Fe-Ga and Cu segments, one can tailor the reversal mechanisms and the switching fields over a wide range of values in Fe-Ga/Cu multilayered nanowires.

CHAPTER 5: REVERSAL MECHANISMS OF SMALL DIAMETER NANOWIRES

5.1 Introduction

Single crystal bulk Galfenol ($Fe_{1-x}Ga_x$, $0.13<x<0.35$) alloys have been known to exhibit magnetostriction constants upto 400 ppm at room temperature,[1] making them next best only to Terfenol-D ($Tb_xDy_{1-x}Fe_y$) alloys.[2] However, unlike Terfenol-D, Fe-Ga alloys are highly ductile and mechanically strong, while possessing several other advantages like high mechanical strength, high magnetization, low hysteresis, low magnetic anisotropy, low saturation fields, and high elastic constants.[3]

As nanowires, these properties make them particularly attractive for transducer and sensor applications. Several studies have used electrochemistry to synthesize large-area, high-density arrays of such Fe-Ga alloy nanowires.[4-9] It has been shown that the electrodeposited Fe-Ga nanowires possess tensile strengths ~2 times that of bulk alloys while being extremely flexible,[10] thus promising high magneto-mechano-electrical coupling when used in microelectromechanical systems (MEMS) and nanoelectromechanical systems (NEMS).[10,11] Practically, however, a fundamental requirement is to be able to rotate the magnetic moments from perpendicular direction to parallel to the nanowires (or vice versa). One way to achieve this is by engineering a ferromagnet/non-magnet (FM/NM) structure that can overcome the shape anisotropy of the nanowires.[12-14]

In this study, 35 nm diameter $Fe_{80}Ga_{20}$/Cu nanowire arrays **(Figure 1(a))** were studied using a vector-enabled vibrating sample magnetometer (vector-VSM), and their magnetic behavior (coercivities and switching mechanisms) were tailored as a function of Fe-Ga and Cu aspect ratios. Varying Fe-Ga segment thicknesses allowed an understanding of the effects of shape anisotropy, and varying the Cu thicknesses led to an understanding of the effects of intra-wire magnetostatic interactions, thus enabling future applications such as artificial cilia, nanoactuators, nanomagnetic sensors, and spintronics.

5.2 Experimental Conditions

The electrolyte consisted of 35 mM Na_3-citrate, 15 mM $FeSO_4$, and 17.5 mM $Ga_2(SO_4)_3$ which were mixed in the same order. The solution pH was adjusted to 3.75 using dilute NaOH. Commercially (Synkera) obtained 35 ± 3 nm diameter anodized aluminum oxide (AAO) templates were used. One side of the templates was sputter-coated with 20 nm Ti adhesion layer followed by 200 nm Au layer. The templates were then annealed at 150 - 200 °C on a hot plate in order to improve the contact. A conventional three-electrode electrodeposition cell was used in which the template acted as the cathode, while a thin sheet of platinum was used as the counter electrode. The depositions were carried at room-temperature under well-stirred conditions creating uniform hydrodynamic conditions near the template surface. Fe-Ga continuous nanowire (structure ‘a’ in Figure 1(a)) deposition was carried under potentiostatic conditions at -1.12 V with respect to Ag/AgCl reference electrode, and resulted in a composition of $Fe_{80}Ga_{20}$ with a growth rate of ~75 nm/min. For Fe-Ga/Cu pulse-deposition,[9] 1.5 mM $CuSO_4$ was added to the above electrolyte and a potential of -0.8 V was used to deposit Cu layers, resulting in ~15 nm/min growth rate. ~19% Cu codeposited during electrodeposition of Fe-Ga layers in the multilayered nanowires, but the Fe:Ga ratio was still found to be 80:20. A JEOL 6500 scanning electron microscope (SEM) equipped with an energy dispersive spectrometer (EDS) was used to measure the elemental compositions. A VSM equipped with vector coils was used for magnetic characterization. Figure 1(b) shows a top view schematic of the VSM. The sample is shown suspended from the vibrating rod positioned between the two magnetic poles (N and S). The two sets of coils surrounding the sample detect variations in x- and y-components of the sample moment (that is, M_x and M_y as shown). The field H_{app} being applied in the x-direction, M_x vs. H_{app} represents the usually obtained hysteresis loops. With the additional set of coils placed in the y-direction, it is possible to simultaneously monitor the variation in M_y component.

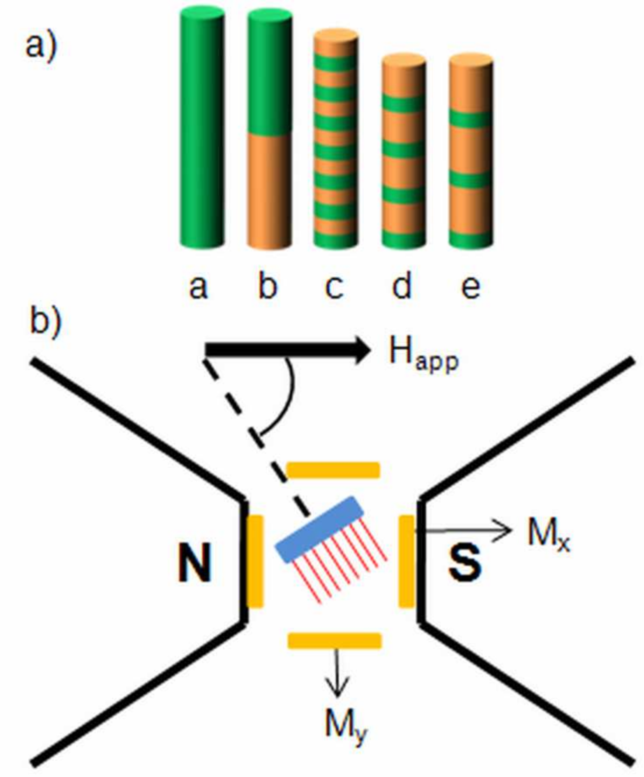

Fig. 5.1. (a) Various 35 nm diameter structures studied in this work. a: [> 55 AR^{FeGa}*], b: [1.0* AR^{FeGa} */ 1.0* AR^{Cu}*]*$_{35}$*, c: [0.1* AR^{FeGa} */ 0.1* AR^{Cu}*]*$_{350}$*, d: [0.1* AR^{FeGa} */ 0.2* AR^{Cu}*]*$_{350}$*, e: [0.1* AR^{FeGa} */ 0.3* AR^{Cu}*]*$_{350}$*. AR = aspect ratio = length/diameter. The subscripts denote number of [*$Fe_{80}Ga_{20}$*/Cu] bilayers. (b) Schematic of top view of VSM showing an additional set of vector coils to measure* M_y *component of the sample moment.*

5.3 Magnetization Reversal Mechanisms

Figure 2 shows room temperature parallel and perpendicular hysteresis loops of all the structures (nanowires embedded within the AAO matrix). The easy axis in each case can be seen to be parallel to the nanowire axis. The fact that even the pancake-like structures ‘c’ - ‘e’ with Fe-Ga aspect ratio of 0.1 still had their easy axis parallel to the nanowire axis pointed to intra-wire magnetostatic interactions, which decreased with increasing Cu thicknesses. In perpendicular fields (Figure 2(b)), structure ‘a’ exhibited a H_{sat} value of approx. 8250 Oe. This was very close to the theoretically expected value of $2\pi M_s \approx 8550$ Oe for infinitely long $Fe_{80}Ga_{20}$ wires, assuming an M_s value of ~1.7 T or 1353 emu/cc for $Fe_{79}Ga_{21}$.[15]

The electrodeposited Fe-Ga nanowires were found to have a disordered bcc *A2* phase, with a strong <011> texture along the nanowire axis and randomized <001> orientation perpendicular to the axis.[9]

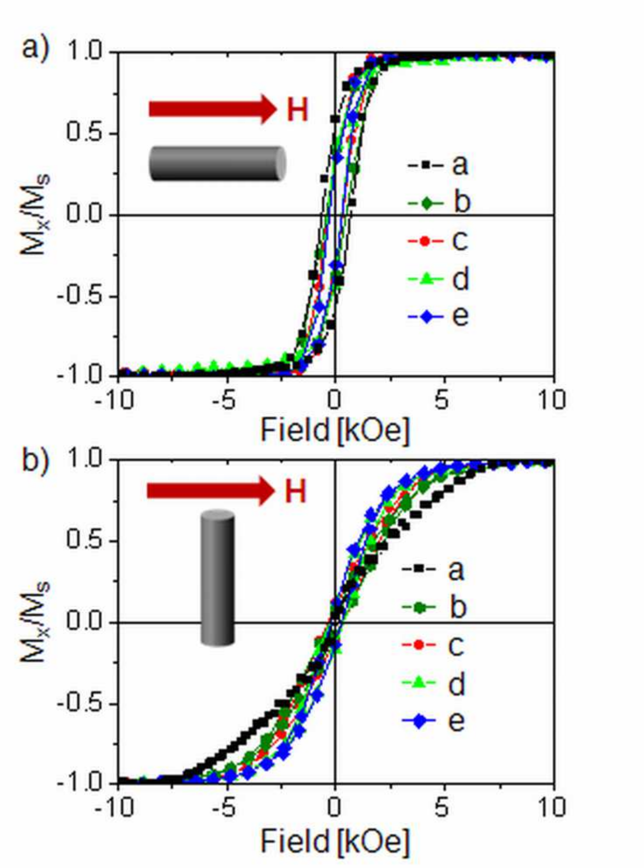

Fig. 5.2. (a) Parallel and (b) perpendicular hysteresis loops of structures 'a' - 'e'.

Therefore, in the absence of significant magnetocrystalline energy in these $Fe_{80}Ga_{20}$ nanowires, the magnetization reversal modes are determined entirely by competition between the exchange energy, the demagnetization energy, and the Zeeman energy.[12] The most common magnetization reversal modes in nanowires are:[16] coherent rotation (CR), in which all the spins rotate coherently; transverse wall (T), in which moments reverse progressively via propagation of a transverse domain wall (*localized* CR mode); curling (C), in which all the moments curl simultaneously; and vortex wall (V), in which the moments reverse progressively via propagation of a vortex domain wall (*localized* C mode). One way to determine which of these modes are occurring during reversal is to study the variation of coercivity (H_c) with the applied field angle.[12] In CR and T modes, H_c values decrease with applied field angles in the 0 - 90° range and result in a minimum at 90° angle, whereas in C and V modes, the H_c values increase continuously resulting in a peak at 90° angle.[12,16]

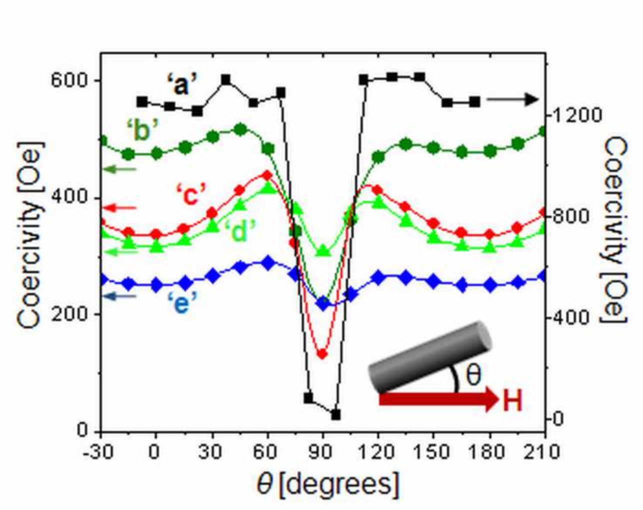

Fig. 5.3. Coercivity as a function of applied field angle for structures 'a' - 'e'.

In a recent study,[9] we reported that 100 nm diameter $Fe_{80}Ga_{20}$/Cu multilayered nanowire arrays undergo reversal by V mode in the entire 0 - 90° angular range. In contrast, the 35 nm diameter structures studied here exhibit increasing H_c values in the low angular range of 0 - 60° followed by a drop to minimum values at 90° angle **(Figure 3)**. This is typical of magnetization reversal occurring by two modes: V mode in the low angular range, and CR mode in the high angular range.[12,16] The result of opposing trends of the two modes is a characteristic peak[12,16] around 60° angles in the coercivity plots. In the low angular range (0 - 60°), the decrease in H_c values with a decrease in the aspect ratio of Fe-Ga segments (in the order, 'a' to 'c') may be attributed to the corresponding decrease in shape anisotropy (note the different vertical scale for 'a').[12] In the high angular range, H_c of structure ‘a’ approached zero at 90°, as one would expect theoretically for an infinitely long cylinder.

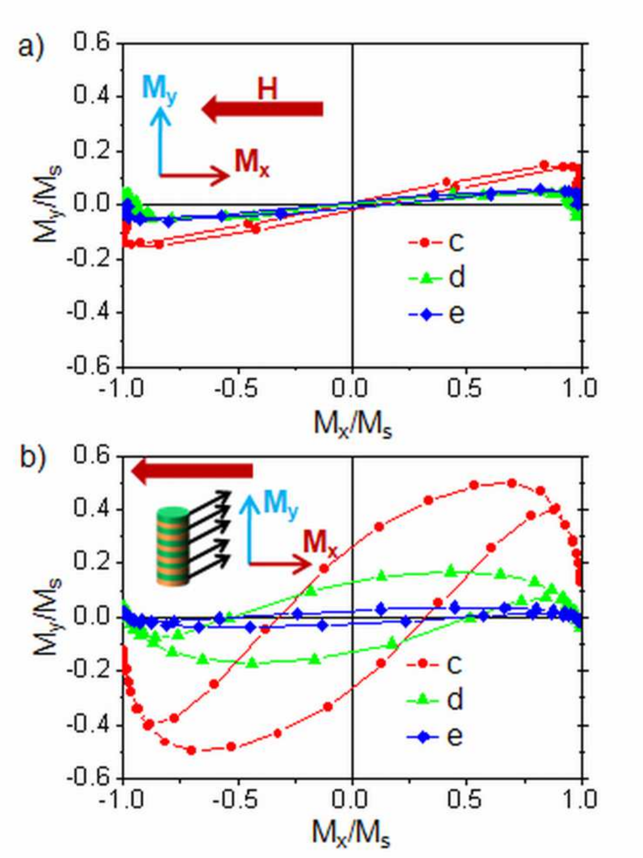

Fig. 5.4. Vector-VSM M_y - M_x plots for (a) parallel and (b) perpendicular applied fields. Schematic in (b) shows the cooperative rotation of moments in adjacent Fe-Ga segments.

In order to use the $Fe_{80}Ga_{20}$/Cu multilayered nanowires for magnetoresistance (MR) or spin-transfer torque (STT) applications, it is of great importance to understand how pancake-like structures ‘c’ - ‘e’ undergo reversal. Vector-VSM was utilized for this purpose **(Figure 4)**. In structures ‘c’ to ‘e’, Fe-Ga aspect ratio was maintained constant at 0.1, but the Cu aspect ratios were increased gradually from 0.1 to 0.3. This allowed a careful investigation of the effect of *intra-wire* magnetostatic interactions on the switching response. At 0° applied field angles (Figure 4a), all of the structures ‘c’ - ‘e’ exhibited relatively negligible M_y components since vortex mode reversal occurs primarily with flux closure. At 90° field angles (Figure 4b), reversal by coherent rotation mode resulted in a significant M_y component. As the Cu thickness increased, the intra-wire magnetostatic interactions decreased, so that the extent to which the moments in adjacent Fe-Ga segments rotate co-operatively decreased. This was clearly reflected by a decrease in the overall M_y component as one goes from structure ‘c’ to ‘e’. From the structures studied here, ‘e’ is the closest but not yet magnetically isotropic. This can be seen in Figures 2-4 with similar M_x vs H_x hysteresis, almost flat angular H_c curves, and negligible M_y (moments follow the applied field). As such, any structure with thicker Cu segments than in ‘e’ presents the best case to be a candidate for magnetostriction-based sensor/actuator applications.

5.4 Conclusions

In summary, we studied the magnetization reversal mechanisms in 35 nm diameter $Fe_{80}Ga_{20}$/Cu multilayered nanowire arrays. It was found that the nanowires undergo reversal by different modes depending on the applied field angles. In the low angular range of 0 - 60°, all structures irrespective of Fe-Ga or Cu aspect ratios underwent reversal by nucleation and propagation of a vortex domain wall. However, in the high angular range, they underwent reversal by coherent rotation mode. It was found that the extent to which moments rotate cooperatively decreased as the Fe-Ga segment separation increased, that is, as the intra-wire magnetostatic interactions decreased.

CHAPTER 6: FeGa/GaAs STRUCTURES FOR SPINTRONICS APPLICATIONS

6.1 Introduction

Among the known magnetostrictive materials, very few show as high a magnetostriction as do Terfenol-D ($Tb_xDy_{(1-x)}Fe_y$)[1] and Galfenol ($Fe_{(1-x)}Ga_x$).[2,3] When compared to Terfenol-D, $Fe_{(1-x)}Ga_x$ alloys possess higher ductility and tensile strength, and lower saturation fields[3] with magnetostrictive constants exceeding 400 ppm at room temperature.[4] These properties make them prime candidates not only for actuator and transducer applications but also for newer technologies like spintronics and multifunctional metal-semiconductor (M-S) hybrid devices. For instance, a recent study[5] proposed to incorporate magnetostrictive M-S structures as functional elements in novel spintronics strain and stress sensors, in which a compressive or a tensile stress is detected by a change in the spin-polarized current. Common techniques to fabricate such structures include molecular-beam epitaxy (MBE), sputtering and chemical beam epitaxy (CBE). Electrochemistry provides an alternative route that is not only economical but is well-suited for large scale fabrication. The feasibility of using electrochemistry to grow epitaxial Fe/GaAs, Bi/GaAs, Co/GaAs, $Fe_{(1-x)}Ni_x$/GaAs structures has been demonstrated in recent studies.[6-10] However, the fabrication and study of the technologically important magnetostrictive $Fe_{(1-x)}Ga_x$/GaAs structures via electrochemistry has not yet been reported, partly owing to the difficult nature of electroplating alloys involving gallium.[11]

Single crystal $Fe_{(1-x)}Ga_x$ alloys exhibit the maximum magnetostriction along <001> direction.[3] However, when $Fe_{(1-x)}Ga_x$ alloy thin films are deposited on polycrystalline brass substrates, either by vacuum deposition techniques[12] or electrochemistry,[11] they tend to have a <011> preferred texture along the growth direction. In this work, we resolve this issue and successfully grow <001> textured $Fe_{(1-x)}Ga_x$ thin films by using a <001> oriented GaAs substrate to influence the growth of the thin films. Furthermore, post growth annealing is used to improve the Fe-Ga/GaAs interface and increase the electron tunneling efficiency. This study can easily be extended to fabricate via electrochemistry other technologically important Heusler alloys that contain gallium, like Fe_2NiGa or Ni_2CoGa.

6.2 Experimental Conditions

Two kinds of substrates were used: polycrystalline brass and epi-ready n-type GaAs (001) (with 2° miscut and Si-doping of ~ 2×10^{17} cm^{-3}). Prior to deposition, the brass substrate surface was cleaned in concentrated HCl for 10 s and rinsed with DI water. The GaAs substrates were dipped into ammonium hydroxide for 30 s to remove the native oxide,[6] rinsed in DI water, and then immediately transferred to the electrolyte. Contact to the GaAs substrate was made by melt-coating a layer of Indium to the backside which was then insulated using Xtal Bond. The electrolyte consisted of 35 mM Na_3-citrate, 15 mM $FeSO_4$, and 17.5 mM $Ga_2(SO_4)_3$ (mixed in the same order) with pH adjusted to 3.75 using dilute NaOH. The counter electrode was a thin sheet of platinum foil. Deposition was carried under a constant applied potential of -1.12 V with respect to Ag/AgCl reference electrode, resulting in a slow growth rate of ~ 1.5 nm/s. A composition of $Fe_{83}Ga_{17}$ was obtained irrespective of the kind of substrate used. X-ray diffraction (XRD) was done using Bruker-AXS Microdiffractometer with 2.2 kW sealed Cu x-ray source. High resolution ω - 2θ scans and rocking curve analysis on GaAs samples were done using Panalytical X'Pert Diffractometer with 1.8 kW sealed ceramic Cu x-ray source. Imaging was done using a

JEOL 6500 scanning electron microscope (SEM) equipped with an energy dispersive spectrometer (EDS) to measure elemental compositions.

6.3 $Fe_{1-x}Ga_x$ Thin Film Deposition

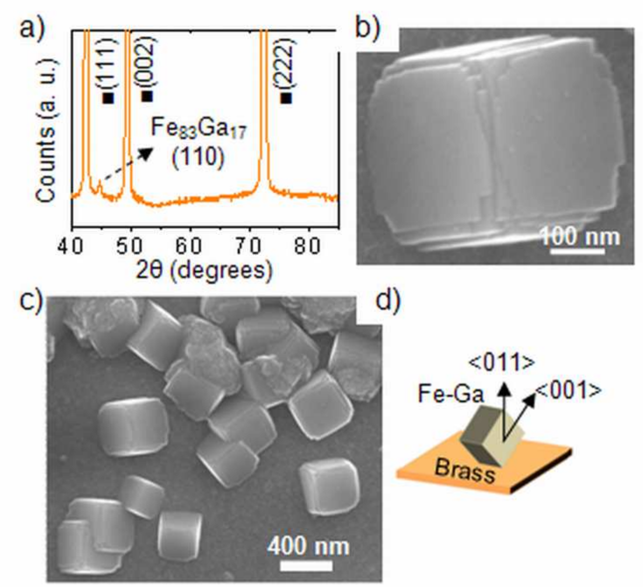

Fig. 6.1. (a) XRD of a $Fe_{83}Ga_{17}$ thin film electrodeposited on brass substrate. (■) symbol represents brass substrate peaks. (b) SEM image showing a single crystal of $Fe_{83}Ga_{17}$ bcc phase nucleated during initial stages of the growth (c) a large scale SEM image showing deterioration of the single crystal growth resulting in polycrystalline growth near the top. (d) Schematic representing orientation of the nucleated crystals relative to the brass substrate.

Figure 1(a) shows a typical XRD pattern obtained for $Fe_{83}Ga_{17}$ thin films electrodeposited on polycrystalline brass substrates. As can be seen, the film was predominantly <011> oriented along the substrate normal. In our previous works, we had reported that this was the case for electrodeposited $Fe_{(1-x)}Ga_x$ thin films over a range of gallium compositions,[11] and also for electrodeposited $Fe_{81}Ga_{19}$ nanowires.[13,14] Figure 1(b) shows an SEM image that captured the initial stages of growth, and one can clearly identify the body-centered cubic (bcc) phase of $Fe_{83}Ga_{17}$. It is well known that electrodeposition occurs by incorporation of adatoms preferentially at step edges and kink sites,[15] resulting in such crystalline growth when conditions are optimum.[16,17] A large scale SEM image (Figure 1(c)) of the same surface shows a number of such cubic crystals randomly nucleated without a preferred in-plane orientation. Figure 1(d) represents the overall <011> preferred orientation of these $Fe_{83}Ga_{17}$ cubic crystals.

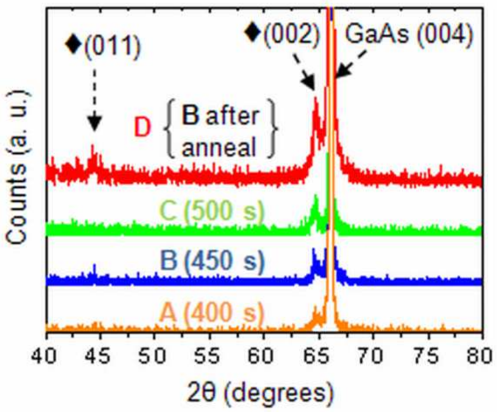

Fig. 6.2. High resolution XRD patterns of Fe-Ga thin films electrodeposited on n-GaAs (001) substrate. Symbol (♦) represents $Fe_{83}Ga_{17}$ film peaks. Electro-deposition time in brackets. XRD pattern D was obtained after sample B was annealed at 300°C for 2 hours in N_2.

In order to avoid the <011> texture, and grow films with the desired <001> texture, one technique is to use a <001> oriented GaAs substrate with a slight miscut. The miscut in the single crystal substrate provides the necessary step edges for nucleation of <001> oriented $Fe_{(1-x)}Ga_x$. As expected, $Fe_{83}Ga_{17}$ thin films electrodeposited on GaAs(001) substrates resulted in a predominantly <001> textured growth **(Figure 2)** with an out-of-plane lattice parameter (d_{001}) of approx. 2.88 nm. Assuming a completely relaxed film, the lattice mismatch between $Fe_{83}Ga_{17}$ and GaAs was then estimated to be at most 1.83%, as opposed to 1.4% for pure Fe on GaAs.[6] As the deposition time, and therefore the film thickness increased in the samples in the order A - C, there was an increase in the <001> peak intensity but without a detectable change in the <011> peak intensity. Upon annealing the sample B at 300°C for 2 hours in N_2 atmosphere (see curve D), the $Fe_{83}Ga_{17}$(002) peak intensity increased significantly, and was accompanied by a now distinguishable but weak $Fe_{83}Ga_{17}$(011) peak.

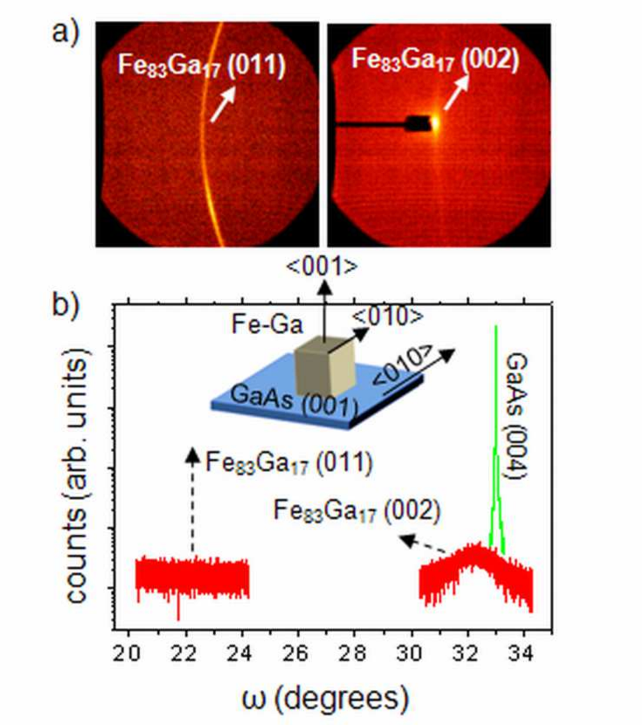

Fig. 6.3. (a) Diffraction patterns for $Fe_{83}Ga_{17}$(002) and $Fe_{83}Ga_{17}$(011) obtained on a 2D area detector in a Laue diffraction mode. The beamstop in right image was used to block the GaAs(004) substrate spot. (b) Separate rocking curves of Fe-Ga (011), Fe-Ga (002) and GaAs

(004) are shown overlaid. Schematic on the top represents the new orientation of the Fe-Ga thin film relative to the GaAs substrate.

For highly textured thin films on single crystal substrates, Bragg-Brentano diffraction mode provides an excellent visual way to analyze the film texture. The bright spot obtained for $Fe_{83}Ga_{17}$ (002) peak on the 2D area detector confirmed the very strong <001> texture in the film (Figure 3(a)). On the contrary, the ring diffraction pattern obtained for $Fe_{83}Ga_{17}$(011) indicated a random orientation of the (011) planes. A further confirmation that the substrate *caused* the <001> texture in the film came from high resolution rocking curve analysis. In Figure 3(b), three separate rocking curves for $Fe_{83}Ga_{17}$(011), $Fe_{83}Ga_{17}$(002) and GaAs(004) are overlaid on the same plot. The $Fe_{83}Ga_{17}$(002) rocking curve exhibited a peak with a full- width half-maximum (FWHM) of 0.7° indicating that the $Fe_{83}Ga_{17}$(002) planes were primarily parallel to the GaAs(001) planes. On the other hand, rocking curve of $Fe_{83}Ga_{17}$(011) did not show any peak implying that the <011> oriented grains resulted only as the film was annealed. Efficient injection of spin-polarized electrons from $Fe_{(1-x)}Ga_x$ films into GaAs is critical for these structures to be used in future spintronic devices.

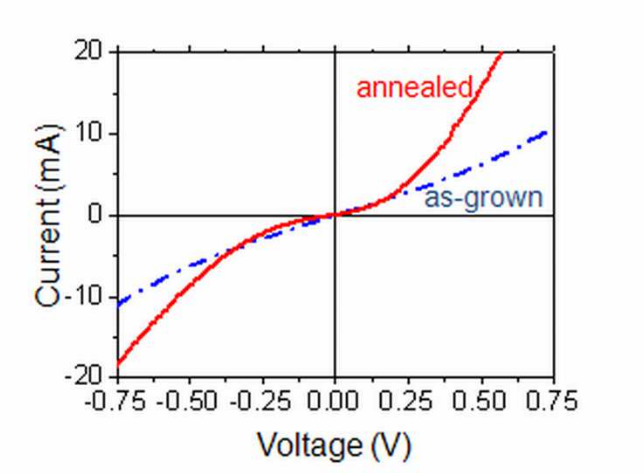

Fig. 6.4. Current - voltage characteristics of $Fe_{83}Ga_{17}$*/GaAs Schottky contacts as-grown and after annealing at 300 °C. All measurements were done at RT.*

Figure 4 shows current - voltage characteristics for the $Fe_{83}Ga_{17}$/GaAs Schottky contacts. The non-linear current-voltage plot obtained for as-grown Fe-Ga/GaAs Schottky contacts was characteristic of tunneling injection. Upon annealing the samples at 300 °C for 2 hours in N_2, a modification of the Fe-Ga/GaAs interface was evidenced by a dramatically improved non-linearity in the current-voltage characteristics. It is to be noted that these results are similar to those obtained for MBE-grown Fe/GaAs structures.[18]

6.4 Summary

In summary, we have studied the influence of polycrystalline brass and single-crystalline GaAs substrates on the texture of electrodeposited $Fe_{(1-x)}Ga_x$ thin films. It was found that $Fe_{83}Ga_{17}$ films grown on brass substrates exhibit a <011> preferential orientation out-of-plane. In contrast, $Fe_{83}Ga_{17}$ thin films grown on GaAs(001) substrates resulted in a strong <001> texture, and high temperature annealing resulted in further improvement of the <001> texture. Rocking curve analysis confirmed that the <001> texture in the $Fe_{83}Ga_{17}$ film was indeed influenced by the GaAs(001) substrate. Current - voltage characteristics obtained revealed an improvement in electron tunneling characteristics upon annealing, thus indicating a modification of the $Fe_{83}Ga_{17}$/GaAs interface.

CHAPTER 7: CONCLUSIONS

A deposition mechanism for $Fe_{1-x}Ga_x$ alloys was proposed in which the formation of an adsorbed monovalent $[Fe(I)]_{ads}$ intermediate was considered to be the rate-determining step. In subsequent steps, this intermediate either gets reduced to iron or catalyses the reduction of gallium by forming an adsorbed $[Ga(III)\text{-}Fe(I)]_{ads}$ intermediate. In fact, induced codeposition of gallium *requires* the formation of this adsorbed intermediate with iron. In line with the proposed mechanism, differences in the mass-transport rates of Fe(II) and Ga(III) species affected the extent of partial current densities i_{Fe} and i_{Ga}, so that by controlling the rotation rate alone, metallic thin film compositions in the entire range of interest (15% - 30% Ga) were obtained.

Electrodeposition of Fe-Ga/Cu multilayered nanowires was accurately controlled by using novel modified RDE-templates together with Cu seed layers and pulsed deposition. The use of a citrate-based electrolytic bath enabled highly textured growth of Fe-Ga segments. Magnetic characterization revealed that in Fe-Ga/Cu multilayered nanowires, the coercivities depended on the aspect ratios, and on the applied field angles. At low applied field angles, the magnetization reversal occurred mainly by the nucleation and propagation of a vortex domain wall. At large applied field angles, a mixed mode of reversal set in, involving a coherent rotation of magnetic moments *within* the Fe-Ga segments and a reversal of vortex structures *at the ends* of the Fe-Ga segments. However, only the latter determined the H_c values at 90° applied field angles, except in structure A with very high Fe-Ga aspect ratio. Thus, by controlling the aspect ratios of Fe-Ga and Cu segments, one can tailor the reversal mechanisms and the switching fields over a wide range of values in Fe-Ga/Cu multilayered nanowires.

Finally, with potential applications in Spintronics, the influence of polycrystalline brass and single-crystalline GaAs substrates on the texture of electrodeposited $Fe_{(1-x)}Ga_x$ thin films was investigated. It was found that $Fe_{83}Ga_{17}$ films grown on brass substrates exhibit a <011> preferential orientation out-of-plane. In contrast, $Fe_{83}Ga_{17}$ thin films grown on GaAs(001) substrates resulted in a strong <001> texture, and high temperature annealing resulted in further improvement of the <001> texture. Rocking curve analysis confirmed that the <001> texture in the $Fe_{83}Ga_{17}$ film was indeed influenced by the GaAs(001) substrate. Current - voltage characteristics obtained revealed an improvement in electron tunneling characteristics upon annealing, thus indicating a modification of the $Fe_{83}Ga_{17}$/GaAs interface.

BIBLIOGRAPHY

CHAPTER 1

[1] S. Peleshanko, M. D. Julian, M. Ornatska, M. E. McConney, M. C. LeMieux, N. Chen, C. Tucker, Y. Yang, C. Liu, J. A. C. Humphrey, and V. V. Tsukruk, Adv. Mater., **19**, 2903-2909 (2007).

[2] D. H. Reich, M. Tanase, A. Hultgren, L. A. Bauer, C. S. Chen, and G. J. Meyer, J. Appl. Phys **93**, 7275-80 (2003).

[3] N. J. Sniadecki, C. M. Lamb, Y. Liu, C. S. Chen, and D. H. Reich, Rev. Scientific Instr. **79**, 044302-1 9 (2008).

[4] A. Hultgren, M. Tanase, C. S. Chen, and D. H. Reich, IEEE Trans. Magn. **40**, 2988-90 (2004).

[5] M. Paunovic and M. Schlesinger, Fundamentals of Electrochemical Deposition, Ed. Hoboken, N.J., Wiley-Interscience, 2006.

[6] G. E. Possin, Physica **55**, 339 (1971).

[7] K. Liu, C. L. Chien, P. C. Searson, and K. Yu-Zhang, Appl. Phys. Lett. **73**, 1436 (1998).

[8] K. Liu, C. L. Chien, and P. C. Searson, Phys. Rev. B **58**, 14681-4 (1998).

[9] Y. Xia, P. Yang, Y. Sun, Y. Wu, B. Mayers, B. Gates, Y. Yin, F. Kim, and H. Yan, Adv. Mater. **15**, 353-389 (2003).

[10] D. Routkevitch, T. Bigioni, M. Moskovits, and J. M. Xu, J. Phys. Chem. **100**, 14037-47 (1996).

[11] D. N. Davydov, P. A. Sattari, D. AlMawlawi, A. Osika, L. Haslett, and M. Moskovits, J. Appl. Phys. **86**, 3983-7 (1999).

[12] C. R. Martin, Science **266**, 1961-1966 (1994).

[13] K. B. Shelimov, D. N. Davydov, and M. Moskovits, Appl. Phys. Lett. **77**, 1722-1724 (2000).

[14] G. Patermarakis and K. Moussoutzanis, J. Electrochem. Soc. 142, 737-743 (1995).

[15] G. Patermarakis, J. Electroanal. Chem. **447**, 25-41 (1998).

[16] L. Ba and W. S. Li, J. Phys. D **33**, 2527-31 (2000).

[17] H. Masuda, H. Yamada, M. Satoh, H. Asoh, M. Nakao, and T. Tamamura, Appl. Phys. Lett. **71**, 2770 (1997).

[18] S. Shingubara, O. Okino, Y. Sayama, H. Sakaue, and T. Takahagi, Solid-State Electron. **43**, 1143 (1999).

[19] O. Jessensky, F. Muller, and U. Gosele, Appl. Phys. Lett. **72**, 1173-5 (1998).

[20] A. P. Li, F. Muller, A. Birner, K. Nielsch, and U. Gosele, J. Appl. Phys. **84**, 6023 (1998).

[21] A. P. Li, F. Muller, and U. Gosele, Electrochem. Solid-State Lett. **3**, 131-4 (2000).

[22] H. Masuda, K. Yasui, Y. Sakamoto, M. Nakao, T. Tamamura, and K. Nishio, Jap. J. Appl. Phys. Lett. **40**, 1267-1269 (2001).

[23] J. Choi, R. B. Wehrspohn, and U. Gosele, Adv. Mater. **15**, 1531-1534 (2003).

[24] B. E. Fischer and R. Spohr, Rev. Modern Phys. **55**, 907-48 (1983).

[25] P. B. Price and R. M. Walker, J. Appl. Phys. **33**, 3400-3406 (1962).

[26] P. B. Price and R. M. Walker, J. Appl. Phys. **33**, 3407-3412 (1962).

[27] C. P. Bean, M. V. Doyle, and G. Entine, J. Appl. Phys. **41**, 1454-9 (1970).

[28] S. K. Chakarvarti and J. Vetter, Nuclear Instr. Methods Phys. Res. B **62**, 109-15 (1991).

[29] L. Sun, C. L. Chien, and P. C. Searson, J. Mater. Sci. **35**, 1097-1103 (2000).

[30] T. Thurn-Albrecht, J. Schotter, G. A. Kastle, N. Emley, T. Shibauchi, L. Krusin-Elbaum, K. Guarini, C. T. Black, M. T. Tuominen, and T. P. Russell, Science **290**, 2126-9 (2000).

[31] L. Sun, Y. Hao, C.-L. Chien, and P. C. Searson, IBM J. Res. Dev. **49**, 79-102 (2005).

[32] P. D. McGary, L. Tan, J. Zou, B. J. H. Stadler, P. R. Downey, and A. B. Flatau, " J. Appl. Phys. **99**, 08B310-6 (2006).

[33] V. P. Parkhutik and V. I. Shershulsky, J. Phys. D **25**, 1258-63 (1992).

[34] R. S. Alwitt and H. Takei, Elsevier, 741 (1983).

[35] D. AlMawlawi, N. Coombs, and M. Moskovits, J. Appl. Phys. **70**, 4421-4425 (1991).

[36] N. J. Gercin, S. S. Mithani, and J. A. Haber, MRS Proc. **879**, 245 (2005).

[37] L. Piraux, J. M. George, J. F. Despres, C. Leroy, E. Ferain, R. Legras, K. Ounadjela, and A. Fert, "Giant magnetoresistance in magnetic multilayered nanowires," Appl. Phys. Lett. **65**, 2484 (1994).

[38] A. Blondel, J. P. Meier, B. Doudin, and J.-P. Ansermet, Appl. Phys. Lett. **65**, 3019 (1994).

[39] K. Liu, K. Nagodawithana, P. C. Searson, and C. L. Chien, Phys. Rev. B **516**, 7381 (1995).

[40] J.-L. Maurice, D. Imhoff, P. Etienne, O. Durand, S. Dubois, L. Piraux, J.-M. George, P. Galtier, and A. Fert, J. Magn. Magn. Mater. **184**, 1-18 (1998).

[41] S. Dubois, L. Piraux, J. M. George, K. Ounadjela, J. L. Duvail, and A. Fert, Phys. Rev. B **60**, 477-84 (1999).

[42] L. Piraux, S. Dubois, C. Marchal, J. M. Beuken, L. Filipozzi, J. F. Despres, K. Ounadjela, and A. Fert, J. Magn. Magn. Mater. **156**, 317-320 (1996).

[43] L. Piraux, S. Dubois, A. Fert, and L. Belliard, Proc. International Conf. Biotech. Pulp Paper Ind. **4**, 413 (1998).

[44] P. R. Evans, G. Yi, and W. Schwarzacher, Appl. Phys. Lett. **76**, 481-483 (2000).

[45] M. Chen, P. C. Searson, and C. L. Chien, J. Appl. Phys. **93**, 8253-8255 (2003).

[46] M. Chen, L. Sun, J. E. Bonevich, D. H. Reich, C. L. Chien, and P. C. Searson, Appl. Phys. Lett. **82**, 3310-3312 (2003).

[47] A. Brenner, Electrodeposition of Alloys, Vol. II, Academic Press, New York (1963).

[48] R. Weil, C. C. Nee, and J. W. Chang, Metallurg. Trans. A **19A**, 1569-73 (1988).

[49] C. C. Nee, W. Kim, and R. Weil, J. Electrochem. Soc. **135**, 1100-3 (1988).

[50] C. Ji, G. Oskam, Y. Ding, J. D. Erlebacher, A. J. Wagner, and P. C. Searson, J. Electrochem. Soc. **150**, 523-528 (2003).

CHAPTER 2

[1] A. E. Clark, K. B. Hathaway, M. Wun-Fogle, J. B. Restorff, T. A. Lograsso, V. M. Keppens, G. Petculescu, R. A. Taylor, J. Appl. Phys. 93 (2003) 8621-8623.

[2] D. J. Bell, T. J. Lu, N. A. Fleck, S. M. Spearing, J. Micromech. Microeng. 15(2005) S153-S164.

[3] N. J. Grabham, N. M. White, S. P. Beeby, Electron. Lett., 36 (2000) 332-334.

[4] D. Iselt, U. Gaitzsch, S. Oswald, S. Fahler, L. Schultz, H. Scholrb, Electrochimica Acta, 56 (2011) 5178-5183.

[5] D. O. Flamini, S.B. Saidman, J.B. Bessone, J. Appl. Electrochem. 37 (2007) 467-471.

[6] N. Eliaz, E. Gileadi, in: C. G. Vayenas, R. E. White, M. E. Gamboa-Aldeco (Eds.), Modern Aspects of Electrochemistry, Springer, New York, 2008, pp. 191-301.

[7] E. J. Podlaha, D. Landolt 144 (1997) 1672-1680.

[8] E. Chassaing, K. Vu Quang, R. Wiart, J. Appl. Electrochem. 19 (1989) 839-844.

[9] M. D. Obradovic, R.M. Stevanovic, A.R. Despic, J. Electroanal. Chem. 552 (2003) 185-196.

[10] E. Beltowska-Lehman, E. Chassaing, J. Appl. Electrochem. 27 (1997) 568-572.

[11] P. D. McGary, B. J. H. Stadler, J. Appl. Phys. 97 (2005) 10R503.

[12] P. D. McGary, K. S. M. Reddy, G. D. Haugstad, B. J. H. Stadler, J. Appl. Phys. 157 (2010) D656-D665.

[13] S. M. Reddy, M. M. Maqableh, B. J. H. Stadler, J. Appl. Phys. 111 (2012) 07E502.

[14] S. M. Reddy, J. J. Park, S. -M. Na, M. M. Maqableh, A. B. Flatau, B. J. H. Stadler, Adv. Func. Mater. 21 (2011) 4677-4683.

[15] S. M. Reddy, J. J. Park, M. M. Maqableh, A. B. Flatau, B. J. H. Stadler, Magnetization reversal mechanisms in 35-nm diameter $Fe_{1-x}Ga_x$/Cu multilayered nanowires, J. Appl. Phys. 2012 (in press).

[16] P. A. Christensen, A. Hamnet, Techniques and Mechanisms in Electrochemistry, first ed., Chapman &Hall, London, 1994.

[17] M. Matlosz, J. Electrochem. Soc. 140 (1993) 2272-2279.

[18] E. Klokholm, IEEE Trans. Magn. 12 (1976) 819.

[19] R.R. Basantkumar, B.J.H. Stadler, R. William, E. Summers, IEEE Trans. Magn. 42 (2006) 3102.

CHAPTER 3

[1] A. Mendelson and R. Tenno, "Modelling and parameter identification of electrochemical Cu-Cu cell," presented at International Conference on Control 2008, UKACC, 2-4 Sept. 2008, Geneve, Switzerland, 2008.

[2] A. Lavacchi, U. Bardi, C. Borri, S. Caporali, A. Fossati, and I. Perissi, J. Appl. Phys. 39 (2009) 2159-2163.

[3] T. J. Davies and R. G. Compton, J. Electroanal. Chem. 585 (2005) 63-82.

[4] T. J. Davies, S. Ward-Jones, C. E. Banks, J. Del Campo, R. Mas, F. X. Munoz, and R. G. Compton, J. Electroanal. Chem. 585 (2005) 51-62.

[5] M. D. Dickey, E. A. Weiss, E. J. Smythe, R. C. Chiechi, F. Capasso, and G. M. Whitesides, ACS Nano 2 (2008) 800-808.

[6] W.-C. Yoo and J.-K. Lee, Adv. Mater. 16 (2004) 1097-1101.

[7] N. Ibl, Comprehensive Treatise of Electrochemistry 6 (1983).

CHAPTER 4

[1] C. Ross, *Ann. Rev. Mater. Res.* **2001**, *31*, 203-235.

[2] X. Huang, L. Tan, H. Cho, B. J. H. Stadler, *J. Appl. Phys.* **2009**, *105*, 07D128.

[3] X. Kou, X. Fan, R. K. Dumas, Q. Lu, Y. Zhang, H. Zhu, X. Zhang, K. Liu, J. Q. Xiao, *Adv. Mater*. **2011**, *23*, 1393-1397.

[4] X. W. Wu, H. Zhou, R. J. M. van de Veerdonk, T. J. Klemmer, C. Liu, N. Shukla, D. Weller, M. Tanase, D. E. Laughlin, *J. Appl. Phys.* **2003**, *93*, 7181-7183.

[5] S. Sun, C. B. Murray, D. Weller, L. Folks, A. Moser, *Science* **2000**, *287*, 1989-1992.

[6] E. C. Walter, K. Ng, M. P. Zach, R. M. Penner, F. Favier, *Microelectron. Eng.* **2002**, *61-62*, 555-561.

[7] T. M. Whitney, J. S. Jiang, P. C. Searson, C. L. Chien, *Science* **1993**, *261*, 1316-1319.

[8] T. Ohgai, X. Hoffer, L. Gravier, J.-E. Wegrowe, J.-P. Ansermet, *Nanotechnology* **2003**, *14*, 978-82.

[9] A. Mourachkine, O. V. Yazyev, C. Ducati, J.-P. Ansermet, *Nano Letters* **2008**, *8*, 3683-3687.

[10] R. Skomski, *J. Phys. Condens. Mat.* **2003**, *15*, R841-R896.

[11] D. H. Reich, M. Tanase, A. Hultgren, L. A. Bauer, C. S. Chen, G. J. Meyer, *J. Appl. Phys.* **2003**, *93*, 7275-7280.

[12] N. J. Sniadecki, C. M. Lamb, Y. Liu, C. S. Chen, D. H. Reich, *Rev. Sci. Instrum.* **2008**, *79*, 044302.

[13] K. M. Ainslie, G. Sharma, M. A. Dyer, C. A. Grimes, M. V. Pishko, *Nano Letters* **2005**, *5*, 1852-1856.

[14] K. M. Ainslie, E. M. Bachelder, G. Sharma, C. A. Grimes, M. V. Pishko, *Nanotoxicology* **2007**, *1*, 279-290.

[15] W. Liang, M. Zhou, F. Ke, *Nano Letters* **2005**, *5*, 2039-2043.

[16] A. E. Clark, M. Wun-Fogle, J. B. Restorff, T. A. Lograsso, *Mater. Trans.* **2002**, *43*, 881-886.

[17] E. Engdahl, in *Handbook of Giant Magnetostrictive Materials*, Academic, New York **2000**.

[18] A. E. Clark, J. B. Restorff, M. Wun-Fogle, T. A. Lograsso, D. L. Schlagel, *IEEE Trans. Magn.* **2000**, *36 (5)*, 3238.

[19] A. E. Clark, M. Wun-Fogle, J. B. Restorff, T. A. Lograsso, J. R. Cullen, *IEEE Trans. Magn.* **2001**, *37 (4)*, 2678.

[20] R. C. Hall, *J. Appl. Phys.* **1959**, *30*, 816-819.

[21] P. R. Downey, A. B. Flatau, P. D. McGary, B. J. H. Stadler, *J. Appl. Phys.* **2008**, *103*, 07D305.

[22] B. A. Evans, A. R. Shields, R. L. Carroll, S. Washburn, M. R. Falvo, R. Superfine, *Nano Letters* **2007**, *7*, 1428-1434.

[23] Z. Zhou, Z. Liu, *J. Bionic Eng.* **2008**, *5*, 358-365.

[24] P. D. McGary, L. Tan, J. Zou, B. J. H. Stadler, P. R. Downey, A. B. Flatau, *J. Appl. Phys.* **2006,** *99*, 08B310.

[25] P. D. McGary, B. J. H. Stadler, *J. Appl. Phys.* **2005**, *97*, 10R503.

[26] N. Lupu, P. Pascariu, C. Gherasim, H. Chiriac, *IEEE Trans. Magn.* **2008**, *44*, 3005.

[27] N. Lupu, H. Chiriac, P. Pascariu, *J. Appl. Phys.* **2008**, *103*, 07B511.

[28] P. D. McGary, K. S. M. Reddy, G. D. Haugstad, B. J. H. Stadler, *J. Electrochem. Soc.* **2010**, *157*, D656.

[29] In private communications.

[30] K. Oikawa, T. Ota, F. Gejima, T. Ohmori, R. Kainuma, K. Ishida, *Mater. Trans.* **2001**, *42*, 2472-2475.

[31] K. Oikawa, T. Ota, T. Ohmori, Y. Tanaka, H. Morito, A. Fujita, R. Kainuma, K. Fukamichi, K. Ishida, *Appl. Phys. Lett.* **2002**, *81*, 5201-5203.

[32] O. Heczko, A. Sozinov, K. Ullakko, *IEEE Trans. Magn.* **2000**, *36*, 3266-3268.

[33] D. J. Sellmyer, M. Zheng, R. Skomski, *J. Phys. Condens Mat.* **2001**, *13*, 433-60.

[34] R. Lavin, J. C. Denardin, A. P. Espejo, A. Cortes, H. Gomez, *J. Appl. Phys.* **2010**, *107*, 09B504.

[35] C. A. Ross, M. Hwang, M. Shima, H. I. Smith, M. Farhoud, T. A. Savas, W. Schwarzacher, J. Parrochon, W. Escoffier, H. N. Bertram, F. B. Humphrey, M. Redjdal, *J. Magn. Magn. Mater.* **2002**, *249*, 200.

[36] C. A. Ross, M. Hwang, M. Shima, J. Y. Cheng, M. Farhoud, T. A. Savas, H. I. Smith, W. Schwarzacher, F. M. Ross, M. Redjdal, F. B. Humphrey, *Phys. Rev. B* **2002**, *65*, 144417.

[37] L. Sun, Y. Hao, C.-L. Chien, P. C. Searson, *IBM J. Res. Dev.* **2005**, *49*, 79-102.

[38] T. Wang, Y. Wang, Y. Fu, T. Hasegawa, H. Oshima, K. Itoh, K. Nishio, H. Masuda, F. S. Li, H. Saito, S. Ishio, *Nanotechnology* **2009**, 19, 455703.

[39] K. Nielsch, R. Hertel, R. B. Wehrspohn, J. Barthel, J. Kirschner, U. Gosele, S. F. Fischer, H. Kronmuller, *IEEE Trans. Magn.* **2002**, *38*, 2571-2573.

[40] X.-T. Tang, G.-C. Wang, M. Shima, *J. Magn. Magn. Mater.* **2007**, *309*, 188-196.

[41] F. Beron, L.-P. Carignan, D. Menard, A. Yelon, *IEEE Trans. Magn.* **2008**, *44*, 2745-2748.

[42] Clime, *Nanotechnology* **2007**, *18*, 435709.

[43] S. Allende, *Nanotechnology* **2009**, *20*, 445707.

[44] M. Bustelo, B. Fernandez, J. Pisonero, R. Pereiro, N. Bordel, V. Vega, V. M. Prida, A. Sanz-Medel, *Anal. Chem.* **2010**, *83*, 329-337.

[45] J. U. Cho, J. H. Min, S. P. Ko, J. Y. Soh, Y. K. Kim, J.-H. Wu, S. H. Choi, *J. Appl. Phys.* **2006**, *99*, 08C909.

[46] L. Trahey, C. R. Becker, A. M. Stacy, *Nano Letters* **2007**, *7*, 2535-2539.

[47] S. Valizadeh, J. M. George, P. Leisner, L. Hultman, *Electrochim. Acta* **2001**, *47*, 865-874.

[48] W.-L. Wang, C.-C. Wan, Y.-Y. Wang, *J. Phys. Chem. B* **2009**, *110*, 12974-12980.

[49] C. Bonhote, D. Landolt, *Electrochim. Acta* **1997**, *42*, 2407-2417.

[50] Cu is not soluble in Fe-Ga, and therefore, a controlled annealing (intentional or otherwise from subsequent processes) would only improve the Fe-Ga/Cu interfaces.

[51] R. Hertel, J. Kirschner, *Physica B* **2004**, *343*, 206.

[52] J. D. L. T. Medina, M. Darques, T. Blon, L. Piraux, A. Encinas, *Phys. Rev. B* **2008**, *77*, 014417.

[53] M. Vazquez, K. Pirota, M. Hernandez-Velez, V. M. Prida, D. Navas, R. Sanz, F. Batallan, J. Velazquez, *J. Appl. Phys.* **2004**, *95*, 6642.

[54] R. Hertel, *J. Magn. Magn. Mater.* **2002**, *249*, 251.

[55] W. Scholz, K. Y. Guslienko, V. Novosad, D. Suess, T. Schrefl, R. W. Chantrell, J. Fidler, *J. Magn. Magn. Mater.* **2003,** *266*, 155-163.

[56] J. J. Park, M. Reddy, C. Mudivarthi, P. R. Downey, B. J. H. Stadler, A. B. Flatau, *J. Appl. Phys.* **2010**, *107*, 09A954.

CHAPTER 5

[1] A. E. Clark, M. Wun-Fogle, J. B. Restorff, T. A. Lograsso, and J. R. Cullen, IEEE Trans. Magn. **37 (4)**, 2678 (2001).

[2] E. Engdahl, *Handbook of Giant Magnetostrictive Materials*, (Academic, New York, 2000).

[3] A. E. Clark, and M. Wun-Fogle, Proc. SPIE **4699**, 421 (2002).

[4] P. D. McGary, and B. J. H. Stadler, J. Appl. Phys. **97**, 10R503 (2005).

[5] P. D. McGary, L. Tan, J. Zou, B. J. H. Stadler, P. R. Downey, and A. B. Flatau, J. Appl. Phys. **99**, 08B310 (2006).

[6] N. Lupu, P. Pascariu, C. Gherasim, and H. Chiriac, IEEE Trans. Magn. **44**, 3005 (2008).

[7] N. Lupu, H. Chiriac, and P. Pascariu, J. Appl. Phys. 103, 07B511 (2008).

[8] J. J. Park, M. Reddy, C. Mudivarthi, P. R. Downey, B. J. H. Stadler, and A. B. Flatau, J. Appl. Phys. **107**, 09A954 (2010).

[9] K. S. Madhukar Reddy, J. J. Park, S. M. Na, M. M. Maqableh, A. B. Flatau, and B. J. H. Stadler, Adv. Func. Mater., 2011, 10.1002/adfm.201101390.

[10] P. R. Downey, A. B. Flatau, P. D. McGary, and B. J. H. Stadler, J. Appl. Phys. **103**, 07D305 (2008).

[11] P. R. Downey, A. B. Flatau, P. D. McGary, and B. J. H. Stadler, Proc. SPIE **6932**, 69320P-1 (2008).

[12] L. Sun, Y. Hao, C.-L. Chien, and P. C. Searson, IBM J. Res. Dev. **49**, 79-102 (2005).

[13] M. Chen, P. C. Searson, and C. L. Chien, J. Appl. Phys. **93**, 8253 (2003).

[14] X.-T. Tang, G.-C. Wang, and M. Shima, J. Magn. Magn. Mater. **309**, 188-196 (2007).

[15] J. Atulasimha, A. B. Flatau, I. Chopra, and R. A. Kellogg, Proc. SPIE **5387**, 487 (2002).

[16] R. Lavin, J. C. Denardin, A. P. Espejo, A. Cortes, H. Gomez, J. Appl. Phys. **107**, 09B504 (2010).

CHAPTER 6

[1] E. Engdahl, *Handbook of Giant Magnetostrictive Materials*, (Academic, New York, 2000).

[2] A. E. Clark, M. Wun-Fogle, J. B. Restorff, and T. A. Lograsso, Mater. Trans. **43**, 881 (2002).

[3] A. E. Clark, J. B. Restorff, M. Wun-Fogle, T. A. Lograsso, and D. L. Schlagel, IEEE Trans. Magn. **36 (5)**, 3238 (2000).

[4] A. E. Clark, M. Wun-Fogle, J. B. Restorff, T. A. Lograsso, and J. R. Cullen, IEEE Trans. Magn. **37 (4)**, 2678 (2001).

[5] J. Atulasimha and S. Bandyopadhyay, J. Phys. D: Appl. Phys. **44**, 205301 (2011).

[6] Z. L. Bao and K. L. Kavanagh, J. Appl. Phys. **98**, 066103 (2005).

[7] Z. L. Bao and K. L. Kavanagh, J. Vac. Sci. Technol. B **24 (4)**, 2138 (2006).

[8] Z. L. Bao, S. Majumder, A. A. Talin, A. S. Arrott, and K. L. Kavanagh, J. Electrochem. Soc. **155**, H841 (2008).

[9] K. L. Kavanagh, Semicond. Sci. Technol. **25**, 024006 (2010).

[10] Z. Liang Bao and K. L. Kavanagh, J. Cryst. Growth **287**, 514 (2006).

[11] P. D. McGary, K. S. M. Reddy, G. D. Haugstad, and B. J. H. Stadler, J. Electrochem. Soc. **157**, D656 (2010).

[12] R. R. Basantkumar, B. J. H. Stadler, W. P. Robbins, and E. M. Summers, IEEE Trans. Magn. **42**, 3102 (2006).

[13] K. S. Madhukar Reddy, J. J. Park, S. M. Na, M. M. Maqableh, A. B. Flatau, and B. J. H. Stadler, Adv. Func. Mater., 2011, 10.1002/adfm.201101390 (in press).

[14] N. Lupu, H. Chiriac, and P. Pascariu, J. Appl. Phys. 103, 07B511 (2008).

[15] E. C. Walter, B. J. Murray, F. Favier, G. Kaltenpoth, M. Grunze, and R. M. Penner, J. Phys. Chem. B **106**, 11407 (2002).

[16] H. Naohara, S. Ye, and K. Uosaki, J. Phys. Chem. B **102**, 4366 (1998).

[17] P. Prod'Homme, F. Maroun, R. Cortes, and P. Allongue, Appl. Phys. Lett. **93**, 171901 (2008).

[18] C. Adelmann, J. Q. Xie, C. J. Palmstrom, J. Strand, X. Lou, J. Wang, and P. A. Crowell, J. Vac. Sci. Technol. **B 23(4)**, 1747 (2005).